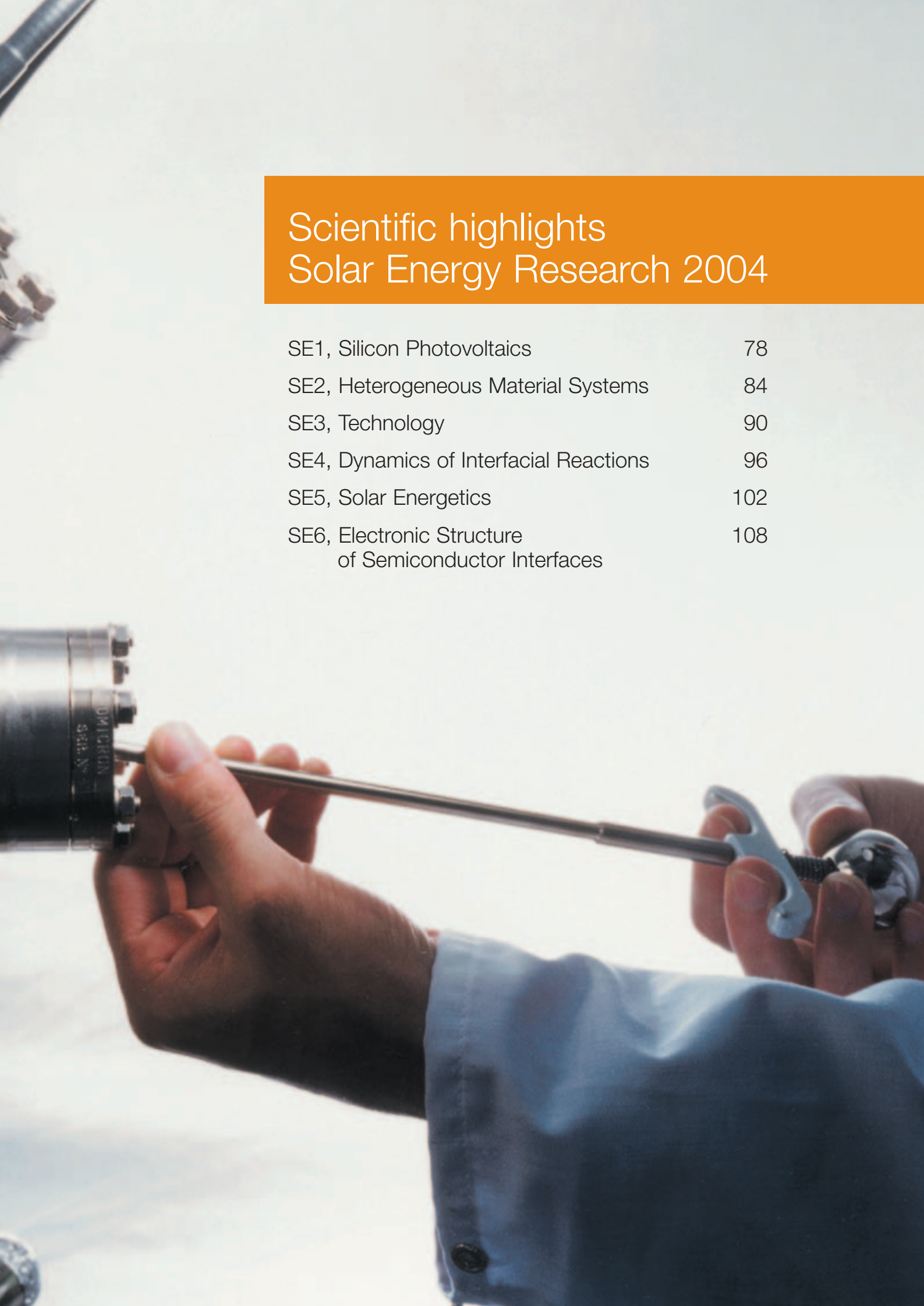


Surface analysis in ultra-high vacuum

A person wearing a white lab coat is shown from the chest up, holding a long, thin metal rod with both hands. The rod is inserted into a complex piece of scientific equipment on the left side of the frame. The person's right hand is holding a blue handle attached to the end of the rod. The background is a bright, slightly blurred white surface. The overall scene suggests a laboratory or research environment.

## Scientific highlights Solar Energy Research 2004

SE1, Silicon Photovoltaics	78
SE2, Heterogeneous Material Systems	84
SE3, Technology	90
SE4, Dynamics of Interfacial Reactions	96
SE5, Solar Energetics	102
SE6, Electronic Structure of Semiconductor Interfaces	108

# Laser-induced self-organization in Si-Ge alloys

M. Weizman, N. H. Nickel, I. Sieber

■ HMI, SE1

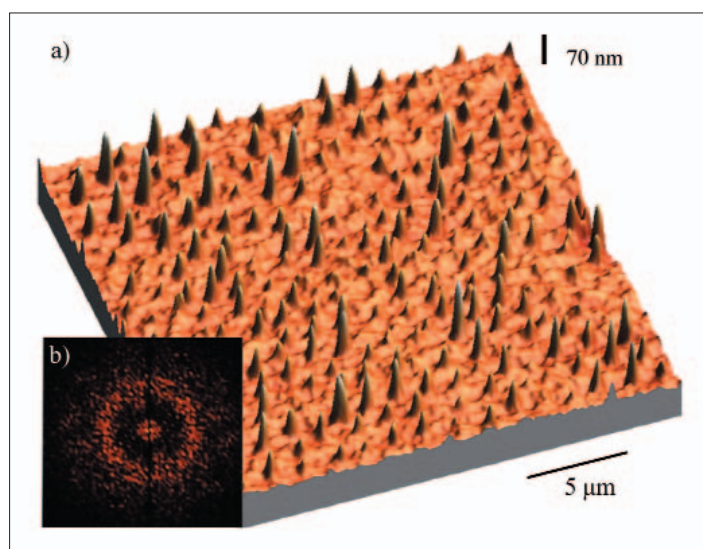


**Fig. 1:** Surface morphology of laser crystallized poly-SiGe  
**a)** Atomic force microscopy (AFM) micrograph  
**b)** Power spectrum of a two-dimensional Fourier analysis of the sample surface

In nature spatial self-organization is a wide spread phenomenon that leads to stunning patterns and structures that can be observed for example in snow flakes and ripples on the beach and sand dunes. Previously, scientists have succeeded to achieve controlled self-organization on much shorter length scales to create novel one- and two-dimensional structures for a new generation of opto-electronic devices. Numerous methods such as solution growth [1, 2], laser-assisted catalytic growth [3], dc sputtering [4], and molecular beam epitaxy [5, 6] have been developed to fabricate self-organized structures. However, all fabrication methods hitherto used are time consuming and require rather high temperatures.

We discovered a laser-induced self-organization of germanium rich dots in silicon-germanium alloys on an ultra short time scale of 100 ns. In addition, the employed method is a low-temperature process where the substrate is held at room temperature.

The silicon-germanium (SiGe) alloys were prepared by the following procedure. At first hydrogenated amorphous silicon-germanium (a-SiGe:H) layers were deposited on quartz substrates by glow-discharge decomposition of silane and germane gas mixtures. Then, the specimens were crystallized employing a XeCl excimer laser operating at a wavelength of 308 nm with a pulse width of about 20 ns. Complete melting and solidification of the samples occurs within about 100 ns. The crystallization experiments were performed at room temperature and in vacuum. The energy distribution of the laser beam was homogenized over an area of  $6 \times 6 \text{ mm}^2$  using a fly's eye homogenizer. Since the a-SiGe:H thin-films contained a hydrogen concentration of up to 13 at.% a step-by-step crystallization technique was applied to avoid ablation of the a-SiGe:H layers. Figure 1a shows an atomic force microscopy (AFM) scan of a poly-Si<sub>0.55</sub>Ge<sub>0.45</sub> sample that was crystallized with a final laser fluence of  $E_L = 650 \text{ mJ/cm}^2$ . While the surface of the amorphous SiGe alloy was smooth the AFM micrograph reveals a quite unusual surface structure of the laser-crystallized specimen. The entire surface is covered with small spikes of a height between 50 and 120 nm. These spikes are not limited to a specific area of the crystallized specimen but occur over the entire surface of the poly-SiGe thin film. The surface micrograph indicates that the distance between spikes is unique. This was verified by applying a two-dimensional Fourier analysis to the AFM micrograph. The resulting power spectrum for the poly-SiGe sample is shown in Fig. 1b. In the reciprocal space a circle with a diameter of  $\approx 1.7 \mu\text{m}^{-1}$  is obtained that corresponds to a mean distance,  $d$ , between spikes of about 1.2  $\mu\text{m}$ .

The composition of the laser crystallized alloys was investigated using energy dispersive X-rays (EDX). The relative Si and Ge signals were calibrated with a single crystal SiGe standard of known composition. Special care was taken to avoid contributions to the silicon signal from the quartz substrate. The amorphous starting material contained a homogeneous Ge concentration of 33%. Laser crystallization caused a significant change of the composition of the polycrystalline specimens. Figure 2a shows an SEM micrograph of the surface of a laser crystallized poly-SiGe sample that was analyzed along the indicated red line using EDX. The white spots represent the laser-induced spikes. The measured Ge content is plotted in Fig. 3b. Surprisingly, the Ge concentration exhibits a sinusoidal variation along the indicated line and varies significantly from the initial 33% of the amorphous starting material. The highest Ge concentration of  $\approx 47\%$  is observed at the spikes (white areas in Fig. 3a). In between the self-organized spikes the Ge concentration decreases to values as low as 27%. This result clearly demonstrates that excimer laser crystallization causes a significant lateral variation of the alloy composition.

The governing mechanism of ultra fast self-organization of SiGe alloys is related to the heating and cooling rates and the presence of germanium. Alloying silicon with germanium has a significant impact on the melting point of the alloy. With increasing Ge content the melting point decreases from 1414°C for pure silicon to 940°C for pure germanium. Melting and solidification during excimer laser crystallization occurs far from thermodynamic equilibrium. In fact, the heating and cooling rates are on the order of  $10^{10}$  K/s. When the entire thin film is melted the liquid SiGe becomes super cooled and subsequently homogeneous nucleation sets in. For pure silicon films with a thickness of 40 nm a nucleation temperature as low as 1130°C was reported [7]. At this time the composition of the SiGe alloy changes abruptly over the entire liquefied area and regions with a lower Ge content than the amorphous starting material and spikes with a high Ge content form. Because of the high cooling rate Ge diffusion into the Ge-depleted regions does not occur.

The self-organization of the spikes occurs because of volume changes of the silicon-germanium alloy during solidification. After nucleation lateral grain growth occurs and the Ge-rich spikes are the last to freeze. Since the liquid material has a higher density than the solid

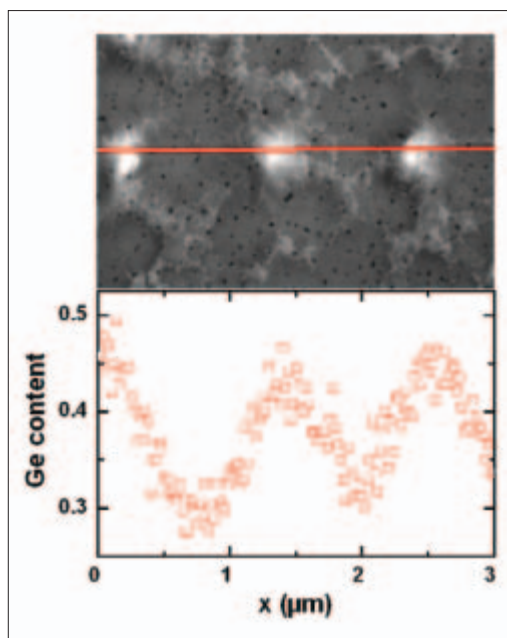


**Fig. 2:** EDX line scan. **a)** Surface micrograph of laser crystallized poly-SiGe. The composition of the laser crystallized SiGe alloy was measured along the indicated red line. **b)** Germanium concentration along the line indicated in **a)**

alloy the growing grains fill a larger volume than the melt they consume. Eventually when the space between grains becomes small the remaining liquid extends above the surrounding layer forming the observed Ge-rich spikes.

- [1] J. D. Holmes, K. P. Johnston, R. C. Doty, B. A. Korgel, *Science* **287**, 1471 (2000)
- [2] Z. Tang, N. A. Kotov, M. Giersig, *Science* **297**, 237 (2002)
- [3] A. M. Morales, C. M. Lieber, *Science* **279**, 208 (1988)
- [4] Y. Zhu, G. S. Cheng, L. D. Zhang, *J. Mat. Science Lett.* **17**, 1897 (1998)
- [5] J. A. Floro, E. Chason, M. B. Sinclair, L. B. Freund, G. A. Lucadamo, *Appl. Phys. Lett.* **73**, 951 (1998)
- [6] C. Teichert, M. G. Lagally, L. J. Peticolas, J. C. Bean, J. Tersoff, *Phys. Rev. B* **53**, 16334 (1996)
- [7] C. P. Grigoropoulos, S.-J. Moon, M.-H. Lee, in *Laser crystallization of silicon*, Ed. N. H. Nickel, (Elsevier – Academic Press, San Diego, 2003), Vol. 75, Chp. 2

**Corresponding author:**  
M. Weizman  
weizman@hmi.de

# Numerical simulation of thin-film heterojunction solar cells: open-source program AFORS-HET, version 1.2

R. Stangl<sup>1</sup>, M. Kriegel<sup>1</sup>, A. Froitzheim<sup>3</sup>, K. v. Maydell<sup>1</sup>, S. Kirste<sup>1</sup>, L. Korte<sup>1</sup>, T. Brammer<sup>4</sup>, H. Stiebig<sup>2</sup>, M. Schmidt<sup>1</sup>

■ 1 HMI, SE1 ■ 2 Photovoltaik-Institut, Forschungszentrum Jülich, Germany ■ 3 present address: Shell-Solar GmbH, München, Germany ■ 4 present address: Q-Cells AG, Thalheim, Germany  
 general contact: AFORS-HET@hmi.de

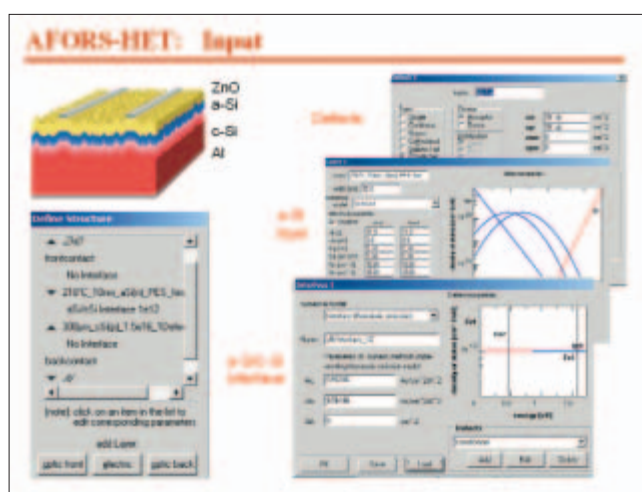


**Fig. 1:** Screenshots of typical AFORS-HET input: Simulation of TCO/a-Si:H(n)/c-Si(p)/Al heterojunction solar cells. (left) layer sequence, (right) density of states of the a-Si:H(n) layer and of the a-Si:H(n)/c-Si(p) interface

We developed a numerical computer simulation program, AFORS-HET, suitable for modelling thin film heterojunction solar cells and the observable of various characterization techniques. It is distributed free of charge via the web site: [www.hmi.de/bereiche/SE/SE1/projects/aSiSi/AFORS-HET](http://www.hmi.de/bereiche/SE/SE1/projects/aSiSi/AFORS-HET)

In order to investigate thin film heterojunction solar cells, a variety of different experimental methods are used, ranging from standard solar cell characterization techniques, like current-voltage (I-V) or quantum efficiency (EQE, IQE) to more advanced characterization techniques, like surface photovoltage (SPV), photo- or electroluminescence (PL, EL), capacitance-voltage (C-V), capacitance-temperature (C-T), impedance (IMP), intensity modulated photocurrent spectroscopy (IMPS) or electrically detected magnetic resonance (EDMR). In order to support the interpretation of such measurements, a numerical simulation

tool, **AFORS-HET**, (automat for simulation of hetero-structures) has been designed. AFORS-HET not only simulates (thin film) heterojunction solar cells, but also the observable of the corresponding characterization techniques. A user-friendly graphical interface allows the visualization, storage and comparison of all simulation data. Furthermore, arbitrary parameter variations and parameter fits to measurements can be performed.

An arbitrary sequence of semiconducting layers can be modelled, specifying the layer and, if needed, interface properties, i.e., the defect distribution of states (DOS). Using Shockley-Read-Hall recombination statistics, the one-dimensional semiconductor equations are solved for thermal equilibrium, various steady-state conditions and for small additional sinusoidal modulations. Additional or modified characterization techniques as well as new numerical modules can be implemented by external users (open-source on demand). Up to now, the following numerical modules have been realized: (a) The front contact can be treated either as a metal/semiconductor contact (Schottky contact) or as a metal/insulator/semiconductor contact (MIS contact). (b) The transport across each semiconductor/semiconductor interface can be modelled either by drift-diffusion currents or by thermionic emission. (c) The optical generation rate can be calculated taking into account coherent and incoherent multiple reflections.

Up to now, we use AFORS-HET mainly to simulate amorphous/crystalline silicon heterojunction solar cells of the structure TCO/a-Si:H(n)/a-Si:H(i)/c-Si(p)/a-Si:H(p<sup>+</sup>)/Al. These solar cells are processed by depositing 5 nm ultra-thin layers of amorphous hydrogenated silicon, a-Si:H, on top of a 300 μm thick crystalline silicon wafer, c-Si. In order to achieve solar cell performance with efficiencies greater than 17%, interface recombination has to be sur-

pressed. Thus, interface sensitive characterization techniques are needed. The corresponding simulations help to interpret the measurements and to compare their sensitivity to the a-Si:H/c-Si interface state density.

Before the calculation, an appropriate sequence of semiconducting layers and interfaces has to be stated (see Fig. 1). For the shown example, the corresponding semiconductor properties, namely the a-Si:H(n) thin-film emitter and the c-Si(p) silicon wafer, must be defined. Additionally, the defect density of states (DOS) has to be specified for all layers and, if needed, for the interfaces.

In order to specify the DOS for the thin-film a-Si:H layers, we use photoelectron yield spectroscopy with UV light excitation (UV-PEYS). With this method the position of the Fermi energy, the density of occupied states in the band gap and the valence band close to the band edge can be measured [1]. As an example, the measured defect distribution of occupied states for a nominal intrinsic and an n-doped a-Si:H layer is shown in Fig. 2. The measured slope of the valence band tail (Urbach energy) and the measured occupied dangling bond distribution are used as direct input parameters in AFORS-HET (compare Fig. 1). However, the Urbach energy of the conduction band tail has to be guessed.

A general interface model assumes a constant DOS of the a-Si:H/c-Si interface with a donor/acceptor behavior in the lower/upper part of the a-Si:H bandgap, respectively (compare Fig. 1). Using AFORS-HET, the sensitivity of various characterization techniques to the a-Si:H/c-Si interface state density can be studied numerically, see Fig. 3, and compared or even fitted to experimental results.

Up to now, approximately 120 AFORS-HET downloads have been recorded, and three updated versions have been published [2]. The program has been used by various groups within the a-Si:H/c-Si community [3–5], mainly in order (1) to evaluate maximum obtainable efficiencies for amorphous/crystalline heterojunction solar cells, (2) to derive design criteria for those solar cells and (3) to develop measurement methods for monitoring the a-Si:H/c-Si interface recombination.

- [1] M. Schmidt, A. Schoepke, L. Korte, O. Milch, W. Fuhs, *The gap state density distribution in extremely thin a-Si:H layers on crystalline silicon wafers*, J. Non-Cryst. Solids **338–340**, 211 (2004)
- [2] R. Stangl, M. Kriegel, K. v. Maydell, L. Korte, M. Schmidt, W. Fuhs, *AFORS-HET, an open source on demand numerical PC program for simulation of (thin film) heterojunction solar cells*, Version 1.2, Proc. IEEE-31, 31<sup>th</sup> IEEE Photovoltaics Specialists Conference, Lake Buena Vista, USA, January 2005, to be published
- [3] A.S. Gudovskikh, J.P. Kleider, R. Stangl, M. Schmidt, W. Fuhs, *Interface properties of a-Si:H/c-Si heterojunctions investigated by admittance spectroscopy*, Proc. 19<sup>th</sup> PVSEC, Paris, France, June 2004, 697
- [4] R. Stangl, D. Schaffarzik, A. Laades, K. Kliefoth, M. Schmidt, W. Fuhs, *Characterization of interfaces in amorphous/crystalline silicon heterojunction solar cells by surface photovoltage spectroscopy*, Proc. 19<sup>th</sup> PVSEC, Paris, France, June 2004, 686
- [5] M. Taguchi, H. Sakata, Y. Yoshimine, E. Maruyama, A. Terakawa, M. Tanaka, *An approach for the higher efficiency in the HIT cells*, Proc. IEEE-31, 31<sup>th</sup> IEEE Photovoltaics Specialists Conference, Lake Buena Vista, USA, January 2005, to be published

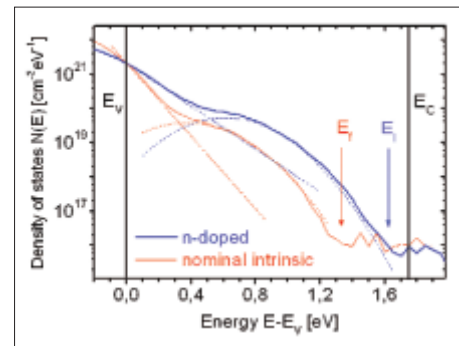


**Fig. 2:** Measured photoelectron yield spectroscopy data for nominal intrinsic and n-doped a-Si:H. The results are used to specify the density of states within the thin amorphous silicon layers.

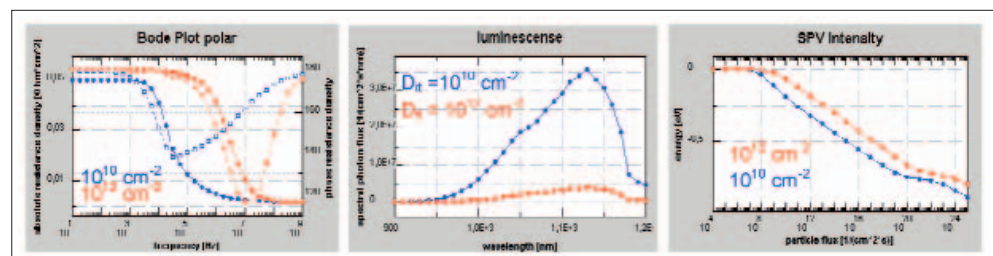


**Fig. 3:** Screenshots of typical AFORS-HET Output: Open-circuit Impedance (left), Photo-luminescence (middle) and illumination intensity dependend Surface Photovoltage (right), simulated for a-Si(n)/c-Si(p) solar cell structures, assuming two different a-Si/c-Si interface state densities  $D_{it} = 10^{10} \text{ cm}^{-2}$  and  $10^{12} \text{ cm}^{-2}$ .

**Corresponding author:**

R. Stangl  
stangl@hmi.de

# Low-temperature Si epitaxy on polycrystalline Si seed layers on glass for thin-film Si solar cells

B. Rau<sup>1</sup>, J. Klein<sup>1</sup>, J. Schneider<sup>1</sup>, M. Muske<sup>1</sup>, E. Conrad<sup>1</sup>, I. Sieber<sup>1</sup>, M. Stöger-Pollach<sup>2</sup>, P. Schattschneider<sup>2</sup>, K. Petter<sup>1</sup>, S. Brehme<sup>1</sup>, S. Gall<sup>1</sup>, K. Lips<sup>1</sup>, W. Fuhs<sup>1</sup>

■ 1 HMI, SE1 ■ 2 Technische Universität Wien, Austria

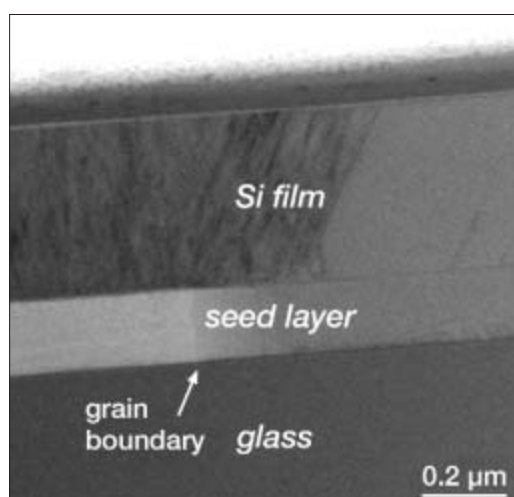


**Fig. 1:** TEM cross-section of a Si film grown on a poly-Si seed layer on glass. Right: epitaxy, left: fine-grained growth, no epitaxy (details see text)

The low-temperature epitaxial thickening of a large-grained polycrystalline Si (poly-Si) film on a foreign substrate like glass is a major challenge on the way to an efficient thin-film solar cell technology with a high potential for cost reduction. In such a concept [1] a thin poly-Si seed layer is used to enable, in principal, crystal growth with lateral grain sizes well above the thickness of the active layer of the solar cell. This seed layer is epitaxially (i. e. under retaining of its crystal information) thickened in a second step to form the absorber layer.

The substrate temperature of all processes involved is limited by the softening temperature of the glass to about 600°C. At these low temperatures it becomes necessary to apply deposition techniques which provide additional non-thermal energy to the surface of the growing film in order to obtain epitaxial growth of Si.

We have shown recently [2] that ion-assisted deposition techniques like electron-cyclotron resonance chemical vapour deposition (ECRCVD) using silane and hydrogen are suitable for epitaxial growth of Si at low temperatures. This technique features a high ion density and a moderate ion bombardment in a remote plasma configuration. Due to the impact of ions onto the growing film and the corresponding momentum transfer the adatom mobility is increased and epitaxial growth is enabled. But in contrast to conventional CVD at high temperatures (~1100°C) the substrate surface conditions (e.g. crystal orientation and surface cleanliness) still influence the epitaxial growth at low-temperatures strongly.

We developed a growth procedure that made it possible for the first time to realise epitaxial growth of Si by ECRCVD on glass based samples [3]. In Fig. 1 a transmission electron microscopy (TEM) sample cross section of a 400 nm thick Si film on a seed layer is given. The image shows the glass substrate (bottom), the seed layer (centre) and the Si film deposited by ECRCVD (top). A region of epitaxial thickening of the seed layer (upper right hand side) and a region of fine-polycrystalline growth (upper left hand side) are shown, caused by two differently oriented grains of the seed layer. The right grain is (100) oriented and has been epitaxially thickened with high crystal quality. The situation is strongly different on the left grain with a crystal orientation tilted with respect to (100). No epitaxy could be obtained here. From investigations of layers grown by ECRCVD on mono- and multicrystalline Si wafers we know, that only a crystal orientation of or close to (100) is favourable for Si epitaxy at temperatures below 600°C [4]. Therefore we used seed layers made by aluminium-induced crystallisation of amorphous Si [5] with a grain size of 10–20 μm and a high degree of (100) orientation. More than

80% of all grains were (100) oriented or were tilted less than  $20^\circ$  with respect to (100). Due to this high degree of preferential (100) orientation of the seed layers, we obtained epitaxy on up to 83% of the total area even at film thicknesses of about  $1.8 \mu\text{m}$ .

The electronic properties of poly-Si thin-film solar cells with grain sizes well above the total thickness of the absorber layer are mainly influenced by intra-grain defects because of their activity as recombination centres for the transversal transport of generated charge carriers. Extended defects like dislocations and stacking faults and other defective regions can be made visible by etching the surfaces of samples by concentrated Secco etch. Secco etch preferentially etches the distorted regions around extended defects. As an example, the resulting etch pits in an epitaxially grown Si film on a monocrystalline Si(100) wafer are shown by a scanning electron microscopy (SEM) top-view image in Fig. 2. Different kinds of etch pits with characteristic shapes, sizes and crystallographic alignments were found. A typical total etch pit density for samples grown at  $560^\circ\text{C}$  is in the range of  $10^8 \text{ cm}^{-2}$ . This high density makes further sample treatments necessary in order to reduce the intra-grain defects (e.g. by rapid thermal annealing) or at least passivate them permanently by hydrogen-treatments.

Nevertheless, first glass/p<sup>+</sup>/p/n<sup>+</sup> solar cell test structures using a slightly boron-doped ECRCVD grown absorber, a low-temperature, highly phosphorous-doped emitter (hydrogenated amorphous Si) and a ZnO film as transparent conducting window layer were prepared. Figure 3 shows the three major stages on the way to the solar cell. On a glass sub-

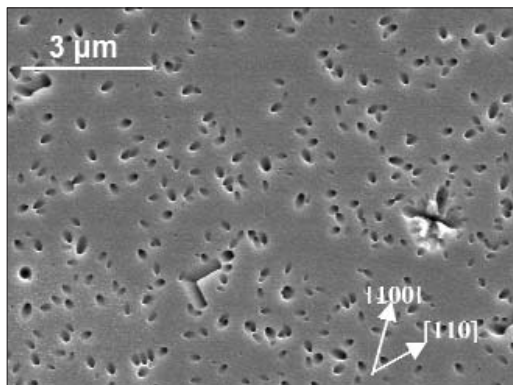


**Fig. 2:** SEM image of a Secco-etched surface of an epitaxially grown Si film (details see text)

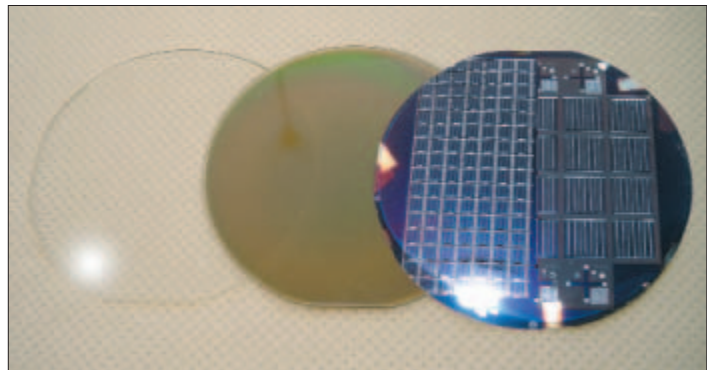


**Fig. 3:** The three major steps to a poly-Si thin-film solar cell on glass (substrate – seed layer – epitaxy and cell processing)

strate (left) a thin poly-Si film was created by metal-induced crystallisation of amorphous Si using the aluminium-induced layer exchange process (ALILE) (centre). This seed layer had now to be epitaxially thickened by ECRCVD to form an approximately  $2 \mu\text{m}$  thick absorber layer. Finally, after emitter and contact deposition, the cells were processed by photolithography (right). With such a structure we obtained first promising results with open-circuit-voltages of up to  $284 \text{ mV}$ . It is expected that an additional rapid high-temperature annealing step of the absorber layer and an effective defect passivation will lead to a strong improvement of the solar cell test structure. This is the challenge for the future work.

- [1] W. Fuhs, S. Gall, B. Rau, M. Schmidt, J. Schneider, *Solar Energy* **77**, 961 (2004)
- [2] J. Schwarzkopf, B. Selle, W. Bohne, J. Röhrich, I. Sieber, W. Fuhs, *J. Appl. Phys.* **93**, 5215 (2003)
- [3] B. Rau, I. Sieber, J. Schneider, M. Muske, M. Stöger-Pollach, P. Schattschneider, S. Gall, W. Fuhs, *J. Crystal Growth* **270**, 396 (2004)
- [4] B. Rau, I. Sieber, B. Selle, S. Brehme, U. Knipper, S. Gall, W. Fuhs, *Thin Solid Films* **451–452**, 644 (2003)
- [5] S. Gall, M. Muske, I. Sieber, O. Nast, W. Fuhs, *J. Non-Cryst. Solids* **299–302**, 741 (2002)

The work has been financially supported by the European Commission (METEOR project, ENK5-CT-2001-00543).

#### Corresponding author:

B. Rau  
bjoern.rau@hmi.de

# Compositional and electronic characterisation of Zn(O,OH) by PES for a better understanding of interfaces in chalcopyrite solar cells

M. Bär<sup>1</sup>, J. Reichardt<sup>1\*</sup>, A. Grimm<sup>1</sup>, I. Kötschau<sup>1</sup>, I. Lauermann<sup>1</sup>, K. Rahne<sup>1</sup>, S. Sokoll<sup>1</sup>, M. C. Lux-Steiner<sup>1</sup>, Ch.-H. Fischer<sup>1</sup>, L. Weinhardt<sup>2</sup>, E. Umbach<sup>2</sup>, C. Heske<sup>3</sup>, C. Jung<sup>4</sup>, W. Gudat<sup>4</sup>, T.P. Niesen<sup>5</sup>, S. Visbeck<sup>5</sup>

■ 1 HMI, SE 2 ■ 2 Exp. Physik II, Universität Würzburg, Germany ■ 3 Dept. of Chemistry, University of Nevada, Las Vegas, USA ■ 4 BESSY Berlin, Germany ■ 5 Shell Solar GmbH, Munich, Germany

\* present address: Institute of Theoretical Physics, University of Bremen, Germany

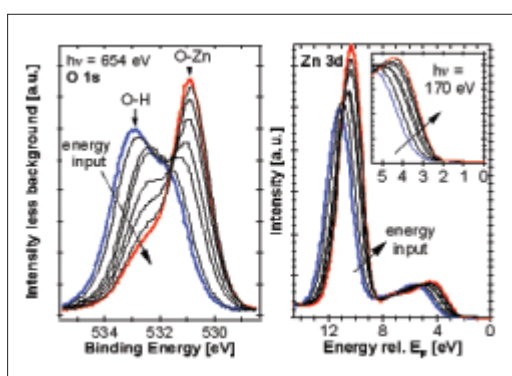


**Fig. 1:** Changes in PES detail spectra of an ILGAR-Zn(O,OH) layer on a CIGSSe absorber due to the energy input of the synchrotron beam (at  $h\nu = 654$  eV).

**left:** O 1s emission at an excitation energy of  $h\nu = 654$  eV.

**right:** Zn 3d emission and the valence band edge (insert) at an excitation energy of  $h\nu = 170$  eV.

Nowadays, the necessity of alternative energy use is widely accepted. In photovoltaic solar energy technology, crystalline silicon cells are currently dominating in the market, though their cost reduction potential is seen to be limited. Thin film solar technology based on the chalcopyrites  $\text{Cu}(\text{In}_{(1-X)}\text{Ga}_X)(\text{S}_Y\text{Se}_{(1-Y)})_2$  ("CIGSSe") with  $0 \leq X \leq 1$  and  $0 \leq Y \leq 1$  is very promising due to expected lower production costs and shorter energy pay back times. Meanwhile, the efficiency of CIGSe based laboratory cells ( $0.408 \text{ cm}^2$ ) has reached almost 20% [1], while industrially produced CIGSSe module prototypes ( $60 \times 90 \text{ cm}^2$ ) have demonstrated efficiencies above 13% [2]. A chalcopyrite-based solar cell is a multilayer system and the quality of the interfaces crucially determines the photovoltaic performance of the cell. Successful interface engineering requires compositional and electronic material characterisation as a prerequisite

for understanding and intentionally generating interfaces. In the following, we present an example for such an approach. Photoelectron spectroscopy with synchrotron radiation is used for both, chemical analysis and determination of the valence band maximum. These data are successfully correlated with the process temperature of the layer deposition as well as with the resulting solar cell efficiencies.

In conventional chalcopyrite solar cells the buffer layer between absorber and window consists of CdS. Despite the small quantity, this is an ecological drawback. Consequently, there is a demand for a non-toxic, more transparent buffer material. One promising approach is the replacement of CdS by a ZnO buffer layer, deposited by the ion layer gas reaction (ILGAR) method. This method has already led to superior cell efficiencies compared to CdS-containing references [3]. Since the chemical, cyclic, and sequential ILGAR deposition of oxide layers occurs via the corresponding hydroxide [4], which is subsequently dehydrated in the heated reaction chamber, the process temperature directly determines the O/OH-ratio of the samples. Therefore, it is possible to prepare ILGAR layers ranging from almost pure  $\text{Zn}(\text{OH})_2$  (deposition at room temperature) to nearly hydroxide-free ZnO (process temperature  $> 200^\circ\text{C}$ ) [5]. Hence, these ILGAR buffers consist of a Zn(O,OH) compound when processed at slightly elevated process temperatures ( $55^\circ\text{C} - 125^\circ\text{C}$ ), as in our case are used. For simplicity, we will still refer to this material as *ILGAR-ZnO*.

Experiments have shown a pronounced drop in solar cell performance when ILGAR-ZnO buffers are prepared above  $100^\circ\text{C}$  [3]. One suggested explanation was a deteriorating impact of an increasing O/OH-ratio, influencing the band alignment at the ILGAR-ZnO/CIGSSe hetero-interface.

In order to study this subject, the O/OH-ratio of ILGAR-ZnO layers was investigated in the CISSY apparatus by means of photoelectron spectroscopy (PES) and correlated with the determined position of the valence band maximum (VBM). An approx. 20 nm thick ILGAR Zn(O,OH) layer, consisting mainly of hydroxide, was irradiated with synchrotron radiation of 654 eV (at the undulator beamline U41-PGM) and the O 1s PES signal was measured in intervals of a few minutes (using a VG CLAM 4 electron analyser). One clearly sees that the oxide peak (530.9 eV) grows at the cost of the hydroxide peak (533.0 eV, peak assignments according to [6]) due to dehydration by the energy input of the synchrotron beam, which also heats the sample. Directly after each O 1s measurement, the excitation energy was tuned to 170 eV and the Zn 3d and valence band signals were recorded (Fig. 1, right). One can observe that the continuous dehydration of the ILGAR-ZnO layer goes along with a shift of the Zn 3d signal from 11.2 eV to 10.4 eV (typical for ZnO [7]) and a shift of the VBM at the surface from 3.8 eV to 2.4 eV. By fitting and integrating the hydroxide and oxide contributions to the O 1s emission, respectively, the ZnO/(ZnO + Zn(OH)<sub>2</sub>) ratio at the surface could be determined.

The corresponding positions of the conduction band minimum (CBM) are estimated using the band gap energies  $E_g$  revealed by optical measurements of respective ILGAR-ZnO layers on glass. CBM and VBM data of the Zn(O,OH) are plotted against oxide content at the surface (Fig. 2, bottom). Previous results from x-ray- (XPS) and UV-light-excited photoelectron (UPS) as well as inverse photoemission spectroscopy (IPES) [6] (full triangles) are in good agreement with CBM and VBM values determined in this way. The dotted lines represent the data for the Cd<sup>2+</sup>/NH<sub>3</sub>-treated CIGSSe substrate [6]. In Fig. 2 (top) the resulting power conversion efficiencies ( $\eta$ ) of ILGAR-ZnO/CIGSSe cells versus the respective buffer compositions are shown. The  $\eta$ -drop may now be directly linked to the ZnO/(ZnO + Zn(OH)<sub>2</sub>) ratio of the buffer. A detailed discussion will be published elsewhere [9]. However, while a predominantly flat conduction band offset (CBO) can be achieved for ZnO/(ZnO + Zn(OH)<sub>2</sub>) ~ 0.56 with a decreasing hydroxide content (assuming that interface-induced band bending effects are negligible), an increasing spike-like CBO above 0.4 eV for oxide-rich ILGAR layers is predicted. The latter may partially (but not exclusively) explain the drop of the power conversion efficiency of resulting solar cells if the ILGAR-ZnO layer is prepared above a process temperature of 100°C, resulting in a hydroxide-poor buffer composition.

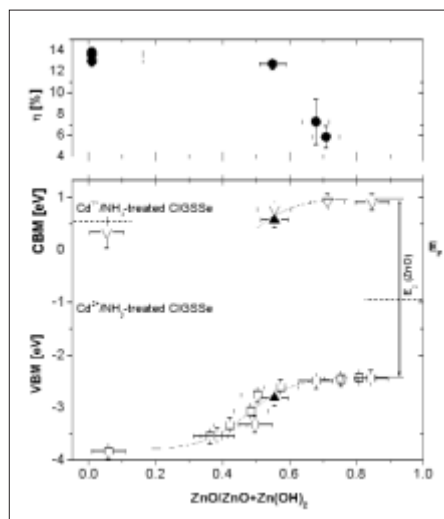


**Fig. 2: bottom:** The determined VBM values (squares) and estimated CBM ( $\approx$  VBM +  $E_g$ ) values (open triangles) of ILGAR-ZnO layers with different ZnO/(ZnO + Zn(OH)<sub>2</sub>) composition compared to previous values [6] for VBM and CBM (directly determined by UPS and IPES, full triangles). The CBM trend line is separated from the VBM trend line by

$E_g(\text{ZnO}) = 3.35 \text{ eV}$  [8]. The dashed lines represent the VBM and the CBM, respectively, of a Cd<sup>2+</sup>/NH<sub>3</sub>-treated CIGSSe absorber [6]. **top:** Power conversion efficiency  $\eta$  of CIGSSe based solar cells with ILGAR-ZnO buffers deposited at different process temperatures [3], shown as function of the Zn(O,OH) composition of the buffer.

#### Acknowledgement

Financial support by the German BMBF (# 01SF0007) and BMWA (# 0329889) is gratefully acknowledged.

- [1] K. Ramanathan, M. A. Contreras, C. L. Perkins, S. Asher, F. S. Hasoon, J. Keane, D. Young, M. Romero, W. Metzger, R. Noufi, J. Ward, A. Duda, *Prog. Photovolt.: Res. Appl.* **11**, 225 (2003)
- [2] V. Probst, Technical Digest of the 14<sup>th</sup> International Photovoltaic Science and Engineering Conference, 2004, p. 663
- [3] M. Bär, Ch.-H. Fischer, H.-J. Muffler, B. Leupolt, T. P. Niesen, F. Karg, M. C. Lux-Steiner, *Proc. 29<sup>th</sup> IEEE Photovoltaic Specialists Conference*, New Orleans, USA, 636 (2002)
- [4] M. Bär, H.-J. Muffler, Ch.-H. Fischer, M. C. Lux-Steiner, *Sol. Energy Mater. Sol. Cells* **67**, 113 (2001)
- [5] Ch.-H. Fischer, H.-J. Muffler; M. Bär, S. Fiechter; B. Leupolt, M. Ch. Lux-Steiner, *J. Crystal Growth* **241**, 151 (2002)
- [6] L. Weinhardt, M. Bär, H.-J. Muffler, Ch.-H. Fischer, M. Ch. Lux-Steiner, T. P. Niesen, F. Karg, Th. Gleim, C. Heske, E. Umbach, *Thin Solid Films* **431–432**, 272 (2003)
- [7] S. W. Gaarenstroom, N. Winograd, *J. Chem. Phys.* **67**, 3500 (1977)
- [8] Landolt-Börnstein, *Halbleiter. II-VI Compounds*, III 22a, Springer Verlag, Berlin (1985)
- [9] M. Bär *et al.*, in preparation

#### Corresponding author:

Ch.-H. Fischer  
fischer@hmi.de

# Time dependent charge separation in a nanoporous $\text{TiO}_2$ model system studied by surface photovoltage

Th. Dittrich<sup>1</sup>, I. Mora-Seró<sup>2</sup>, J. Bisquert<sup>2</sup>

■ 1 HMI, SE2 ■ 2 Departament de Ciències Experimentals, Universitat Jaume I, Castello, Spain

Spatial charge separation is important in many biological, chemical and physical systems and can take place at extremely different time and length scales depending on the investigated system. For example, charge separation may proceed within tens of fs during ultra-fast injection from dye molecules into  $\text{TiO}_2$  [1] or over long times during diffusion in a porous semiconductor [2]. On the other side, light-induced charge may be separated over distances between molecules up to the range of space charge regions. In devices such as nanostructured solar cells [3] or so-called eta (extremely thin absorber) solar cells, it is important to clarify the time and length scales at which the related processes of initial charge separation, carrier transport and recombination take place.

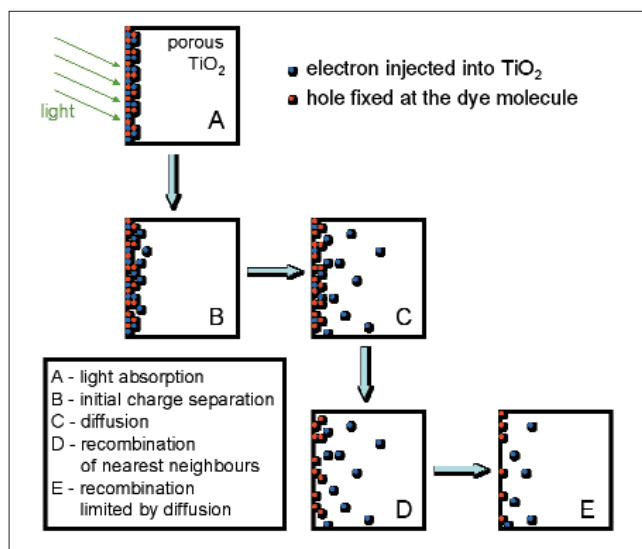


**Fig. 1:** Scheme of elementary processes in the investigated model system consisting of a nanoporous  $\text{TiO}_2$  layer sensitized with dye molecules near the surface. In addition, di-electric relaxation has to be considered. The nanoporous  $\text{TiO}_2$  can be treated as an effective medium. The photovoltage is given by the amount of separated charge and by the effective charge separation length.

In contrast to time dependent optical investigations, surface photovoltage (SPV) measurements give information about both time *and* length scales of charge separation. This opens the opportunity to measure transport phenomena from the ns to the s range with excellent sensitivity. Figure 1 summarizes elementary processes dominating charge separation at extremely different time scales for a model system in which the positive light induced charge remains fixed near the surface and only electrons are mobile. In our SPV studies, the processes B–E were clearly distinguished.

Recently, SPV measurements were performed on different electron and hole conductors with adsorbed N3 ( $\text{Ru}(\text{dcbpyH}_2)_2(\text{NCS})_2$ ) dye molecules [4]. Further, it has been shown that N3 dye molecules adsorbed at  $\text{TiO}_2$  surfaces are very stable in vacuum at relatively high temperatures [5]. Following this experience, we realized a model system, similarly to the system shown in Fig. 1, for time and temperature dependent SPV measurements on nanoporous  $\text{TiO}_2$ .

Nanoporous  $\text{TiO}_2$  layers of interconnected anatase nanoparticles (diameter of the particles about 16 nm) were deposited on glass coated with conducting  $\text{SnO}_2:\text{F}$ . Only the surface region of the nanoporous  $\text{TiO}_2$  layers was sensitized with dye molecules by short dipping in the dye solution. Spectral surface photovoltage measurements showed the typical absorption behavior of the N3 dye molecules.

SPV measurements were carried out in the capacitor arrangement with a thin mica layer as spacer. Light pulses of the 2<sup>nd</sup> harmonic of a Nd:YAG laser (wavelength 531 nm, duration time 120 ps) were used for excitation. At this wavelength, the light was absorbed only by N3 dye molecules but not by  $\text{TiO}_2$  nanoparticles. The resolution time of the whole system was better than 2 ns. Before starting the SPV measurements, the sample was conditioned inside the evacuated cryostat at 270°C for 30 min.

Figure 2 shows examples for SPV transients in linear-log and log-log scales for a nanoporous  $\text{TiO}_2$  layer sensitized with N3 dye molecules near the surface. The SPV transients were measured at different temperatures for quite low excitation intensity. The SPV signals increase in time, reach a characteristic maximum at times much longer than the laser pulse and decay. The characteristic maximum depends strongly on temperature and is determined mainly by dielectric relaxation.

The increase at the shorter times as well as the decrease at the long times (for higher temperatures) of the SPV transients follow power laws (Fig. 2b). The power laws indicate diffusion and dispersive transport during increasing charge separation length due to independent diffusion and during decreasing charge separation due to recombination limited by diffusion (processes C and E in Fig. 1), respectively. As remark, the power coefficients can be well interpreted in traditional time-of-flight experiments where the displacement current is measured. The situation is much more complicated for the interpretation of SPV transients. The creation of a sophisticated model and simulations of SPV transients are a great challenge for future.

At a fixed intensity of the laser pulse, the extrapolated on a log-log scale SPV transients have a common point of intersection for the different temperatures. The time at the point of intersection is independent of the intensity of the laser pulse and amounts to about 100 ps, i.e. the duration time of the laser pulse. At this time, the extrapolated SPV signal scales linearly with the intensity of the laser pulse. Therefore, dispersive transport sets on within the laser pulse and a respective initial charge separation length of 3–10 nm has been estimated (process B in Fig. 1) [6]. Further, the power-law approximation may open new opportunities for the investigation of initial charge separation at ultra-short times if working with much shorter laser pulses.

The fastest relaxation process of the SPV signal can be described by a logarithmic decay which probably indicates to recombination between nearest neighbors, i.e. to limitation by tunneling over a variable range of distances (process D in Fig. 1). A logarithmic decay time ( $\tau_{\text{LN}}$ ) can be defined (see the example in Fig. 2b).

At higher temperatures,  $\tau_{\text{LN}}$  is thermally activated and independent of the intensity of the laser pulse [6]. The values of the activation energy and of  $\tau_{\text{LN}}^0$  are 0.65 eV and 2 ps, respectively. The observed activation energy is typical for the thermally activated conductivity in  $\text{TiO}_2$ . This gives further evidence that the decay of the SPV transients is limited by the electron transport. The obtained value  $\tau_{\text{LN}}^0 = 2 \text{ ps}$  is typical for multiple trapping, for example in amorphous Si, and it reflects the shortest possible time for charge transfer of an electron back into a charged dye molecule. Of course, this time may be much longer than the electron transfer from the adsorbed dye molecule into the  $\text{TiO}_2$  nanoparticle [1].

We demonstrated that the SPV technique is a powerful tool to obtain information about spatial charge separation in a wide range of time scales from ps to s. Besides the signatures for diffusion and dispersive transport, a logarithmic decay was observed for photovoltage transients in porous  $\text{TiO}_2$  sensitized at the surface with dye molecules [6].

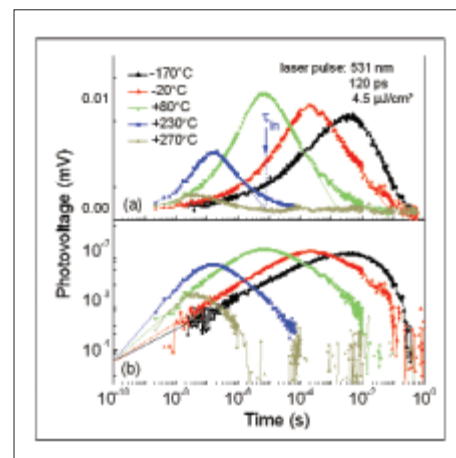


**Fig. 2:** SPV transients in linear-log (a) and log-log (b) plots for a nanoporous  $\text{TiO}_2$  layer sensitized with dye molecules near the surface. The repetition rate of the laser pulses was 1 Hz.

- [1] see, for example, K. Schwarzburg, R. Ernstdorfer, S. Felber, F. Willig, *Coordination Chemistry Review* **248**, 1259–1270 (2004), and refs. therein
- [2] V. Duzhko, V. Yu. Timoshenko, F. Koch, Th. Dittrich, *Phys. Rev. B* **64**, 0752041–0752047 (2001)
- [3] M. Grätzel, *Nature* **414**, 338–344 (2001) and refs. therein
- [4] B. Mahrov, G. Boschloo, A. Hagfeldt, L. Dloczik, Th. Dittrich, *Appl. Phys. Lett.* **84**, 5455–5457 (2004)
- [5] Th. Dittrich, *phys. stat. sol. (a)* **201**, R69–R71 (2004)
- [6] Th. Dittrich, I. Mora-Sero, J. Bisquert, submitted

#### Corresponding author:

Th. Dittrich  
dittrich@hmi.de

# Electrical activity at grain boundaries of Cu(Ga, In)Se<sub>2</sub> thin films

D. Fuertes Marrón<sup>1</sup>, S. Sadewasser<sup>1</sup>, A. Meeder<sup>2</sup>, Th. Glatzel<sup>1</sup>, M. Ch. Lux-Steiner<sup>1</sup>

■ 1 HMI, SE2 ■ 2 SULFURCELL Solartechnik GmbH

In comparison to grain boundaries (GBs) in Si, those in chalcopyrite semiconductors are by far not as well studied nor understood. Only very recently have some experimental and theoretical studies been conducted, motivated by the remarkably high solar energy conversion efficiencies of polycrystalline absorbers compared to those obtained so far from single-crystalline ones. Reaching efficiency figures close to 20% from any type of polycrystalline absorber (including as well Si or CdTe) necessarily requires a favourable behaviour of the GBs. Experimental studies have demonstrated electrical effects at p-type chalcopyrite GBs, both indirectly by Hall and conductivity measurements and directly using Kelvin probe force microscopy (KPFM); results were explained according to a GB model developed for Si, which assumes a depletion layer in the near-GB region induced by some charge storage at interface states.

This bends the bands downwards some 100 meV, representing an electrostatic barrier for the transport of holes (typically majority carriers) and a sink for electrons (minority ones). The depletion region on either side of the GB plane results from positively charged interface states. The minor detrimental role attributed to GBs in polycrystalline thin-film solar cells is accounted for within the frame of this *electronic* GB model by a certain reduction of the band bending at the GBs gained under illumination (i.e. under solar cell operating conditions), as a fraction of minority carriers are trapped at interface states, reducing the net stored charge and thus the associated electric field and depletion region.

In contrast to the *electronic* GB model, a recent theoretical study using first-principles modelling of GBs for selected grain orientations in CuInSe<sub>2</sub> proposed the appearance of an energetic barrier for holes arriving from the inner part of the grains without the presence of interface charge at GBs. A reduced *p-d* hybridization between group-I-cation and chalcogen-anion states, due to Cu-vacancy surface reconstruction, was proposed to lead to an overall downward shift of the valence band maximum in the near-GB region. This model can indeed account for the experimental observations based on electronic transport measurements mentioned above. The absence of available free holes at GBs prevents electron recombination, minimizing the detrimental effects for electronic applications as a result of minority carrier loss. This *structural* GB model explicitly excludes built-in potentials (i.e. stored charge) at GBs. This is understood as the result of a self-compensation of electronic point defects by their arrangement into neutral pairs of the type  $2V_{-Cu} + In^{2+}_{Cu}$ .

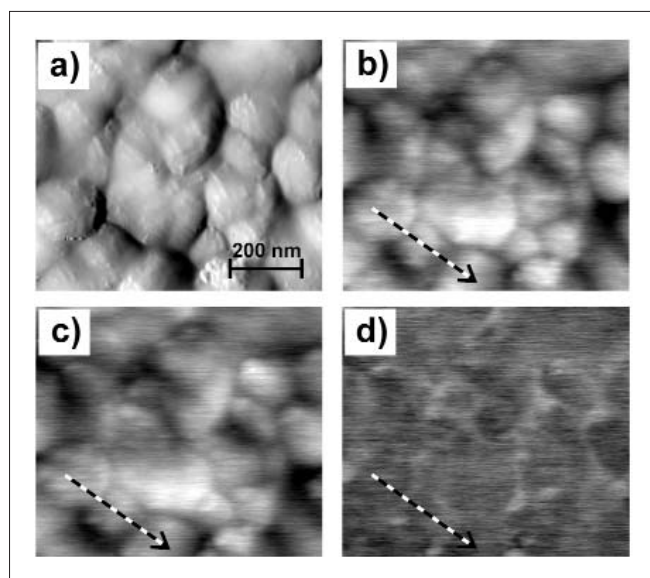


**Fig. 1:** KPFM measurement on the UHV-clean rear side of a CuGaSe<sub>2</sub> absorber film. **a)** Topography (height range = 92 nm), **b)** work function in dark (4.79–4.94 eV), **c)** work function under illumination (4.88–5.01 eV), and **d)** SPV image (41–140 mV). Different GB types are distinguished by the presence or absence of SPV. The line represents the position of the line scan in Fig. 2.

To investigate the applicability of the two GB models, we used KPFM in ultra-high vacuum (UHV) to study polycrystalline CuGaSe<sub>2</sub> (CGSe) thin-film samples grown in a two-stage process by chemical vapour transport onto Mo-coated soda-lime glass. Samples were peeled-off in UHV in order to expose a clean rear surface to the tip.

The topography image of the CGSe rear surface (Fig. 1a) shows a granular texture, corresponding to the base of columnar grains ( $\sim 3\ \mu\text{m}$  long) with lateral dimensions between 50–400 nm; in contrast, typical grain widths at the film top surface lie in the micrometer range. GBs can be identified in the work function mapped in the dark in Fig. 1b by direct inspection and comparison to the topographical image, showing lower work function values than the crystallite surfaces. This effect is clearly seen along a representative line-scan shown in Fig. 2. Three adjacent grains build up GBs A and B. The work function lowering associated with the GBs is different in magnitude by a factor of approximately two. Due to the flat topography of the absorber's rear surface (height range  $\sim 90\ \text{nm}$ ), any possible influence of surface roughness on the work function measurement can be largely excluded. This work function reduction at GBs as recorded in the dark is however not sufficient to favour the *structural* or the *electronic* GB model.

Thus, we additionally studied the electronics at energies above the Fermi level, i. e., the changes observed in the electrical activity at GBs induced by excess electrons, acting as minority carriers. If GBs were governed by *structural* (i. e., band offsets) rather than *electronic* (built-in potential) factors as described by the models, the impact of the excess minority carriers should only be minor. Illuminating the sample with super-bandgap light (laser diode,  $\lambda = 675\ \text{nm}$ ) results in an overall increase of the work function (Fig. 1c) which saturates at high intensities ( $\sim 60\ \text{mW}/\text{cm}^2$ ), an effect attributed to a reduction of the surface band bending in the scanned (sample-vacuum) surface plane. In Fig. 1d a surface photovoltage image ( $\text{SPV} = \Phi^{\text{ill}} - \Phi^{\text{dark}}$ ) of the scanned area is presented, obtained by subtracting Fig. 1b (measured in the dark) from Fig. 1c (under illumination), which shows the presence of at least two distinct GB types, one showing a larger SPV than the grains (bright areas) and others which do not show up. A representative line scan in Fig. 2 shows a significant reduction of the work function drop recorded at GB B under illumination, together with the overall increase in work function attributed to SPV on the scanned surface plane; this shows up as a characteristic peak in the SPV line (bottom). At the same time, GB A shows almost no change under illumination. This leads us to conclude the existence of different types of GBs, presumably associated with particular crystallite orientations. This connection between crystallite orientation and GB electrical activity can explain the influence of

film texturing on the performance of high efficiency solar cells, in addition to a favourable band alignment between absorber and buffer layers, a point which has not yet received sufficient attention and which may in our opinion be of fundamental importance for further device optimisation.

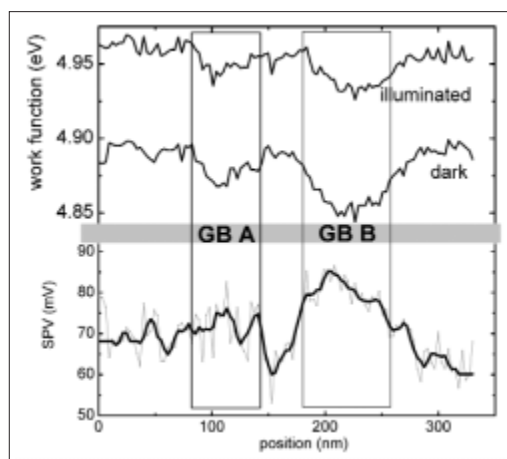


**Fig. 2:** Line scan along the line in Fig. 1. Upper panel: A drop in the work function (in dark and under illumination) at the position of the GBs is observed. GBs A and B are of different types as indicated by their different SPV characteristic (lower panel); the line is a smoothed curve of the data (gray line).

The reduction of the potential barrier at GBs associated with illumination cannot be accounted for within the frame of the *structural* GB model under the exclusive premise of an interface dipole. The decrease of the work function fits however into the *electronic* GB model: a reduction of the potential barrier is due to photo-generated minority carriers (electrons) being trapped at ionised donor-like electronic states at the GB. The mechanism of light-induced GB passivation within the *electronic* GB model does not seem to apply equally to all types of GBs. For example, the behaviour of GBs of type A, which shows almost no change under illumination, might well be explained to a large extent by the *structural* GB model. On the other hand, the illumination induced change in the GB of type B does require the *electronic* GB model.

This work was financially supported by the German Ministry for Research and Education (Contract No. 01SF0023).

This work has been published in Phys. Rev. B **71**, 033306 (2005)

**Corresponding author:**  
D. Fuertes Marrón  
fuertes-marron@hmi.de

# Production of $\text{CuInS}_2$ baseline modules on $5 \times 5 \text{ cm}^2$ substrates with high yield

J. Klaer<sup>1</sup>, R. Klenk<sup>2</sup>, R. Scheer<sup>1</sup>, H.-W. Schock<sup>1</sup>

■ 1 HMI, SE3 ■ 2 HMI, SE2

Research in the department SE3 is focussed on the technology of thin-film photovoltaic devices with absorbers based on chalcopyrite compound semiconductors. A baseline process has been developed for the preparation of  $\text{CuInS}_2$  solar cells and mini modules up to  $10 \times 10 \text{ cm}^2$  in size. Samples originating from this baseline process are used for research on special questions and development of single process steps. For many purposes small area single cells are the adequate type of device.

In the face of future commercial application, modules are of particular interest. Additional process steps are necessary to fabricate modules that normally are not needed for single cells, e.g. integrated series connection and encapsulation. In 2003 the company Sulfurcell has been founded by the Hahn-Meitner-Institut scientists in order to fabricate commercial modules based on the process developed in the department SE3. A corporation contract between the Hahn-Meitner-Institut and Sulfurcell provides scientific support from the Hahn-Meitner-Institut.

Against this background it is of special importance to maintain a continuous fabrication of mini-modules in the SE3 baseline. This allows a consecutive process control and improvement of module related process steps. Additionally it is a proof of the stability of the process, an essential item for industrial suitability.

From July to December 2004 in total 128 modules have been fabricated on  $5 \times 5 \text{ cm}^2$  glass substrates. Figure 1 shows the yield of the fabrication process for these modules: the blue histogram gives the number of modules in efficiency intervals of 0.1 %, respectively, while the red curve gives the accumulative yield. Only 10 modules have efficiencies less than 6.9%, the best module is close to 10 %, and the maximum of the distribution shows at 9%. According to the red curve, modules with 8% efficiency have been produced at a yield of about 75%, which means that 75% of all modules fabricated have efficiencies of 8% or more. For 7% modules the yield is about 90%.

Only modules produced with baseline parameters are included within the 128 modules shown in Fig. 1. Baseline devices, both solar cells and modules, are processed with well defined process parameters that have been evaluated as optimum and set as a standard. Besides these baseline devices a large number of additional samples with deliberately deviating process parameters have been processed. These experiments are essential in the context of research and process development, but they result in samples that are not relevant within a baseline statistics.

During the first 6 months of 2004 the efficiency distribution was much broader compared to Fig. 1, showing many modules with only poor or moderate efficiencies. This poor statistics can be attributed to various problems with processing that meanwhile could be solved. This underlines the necessity of continuous module preparation for process improvement.

Additionally to the devices on  $5 \times 5 \text{ cm}^2$  substrates a couple of  $10 \times 10 \text{ cm}^2$  modules have also been processed. Its number is too small to give meaningful statistics, but the best  $10 \times 10 \text{ cm}^2$  module has achieved 8.9% efficiency so far. An example of such a module already encapsulated is shown in Fig. 2.

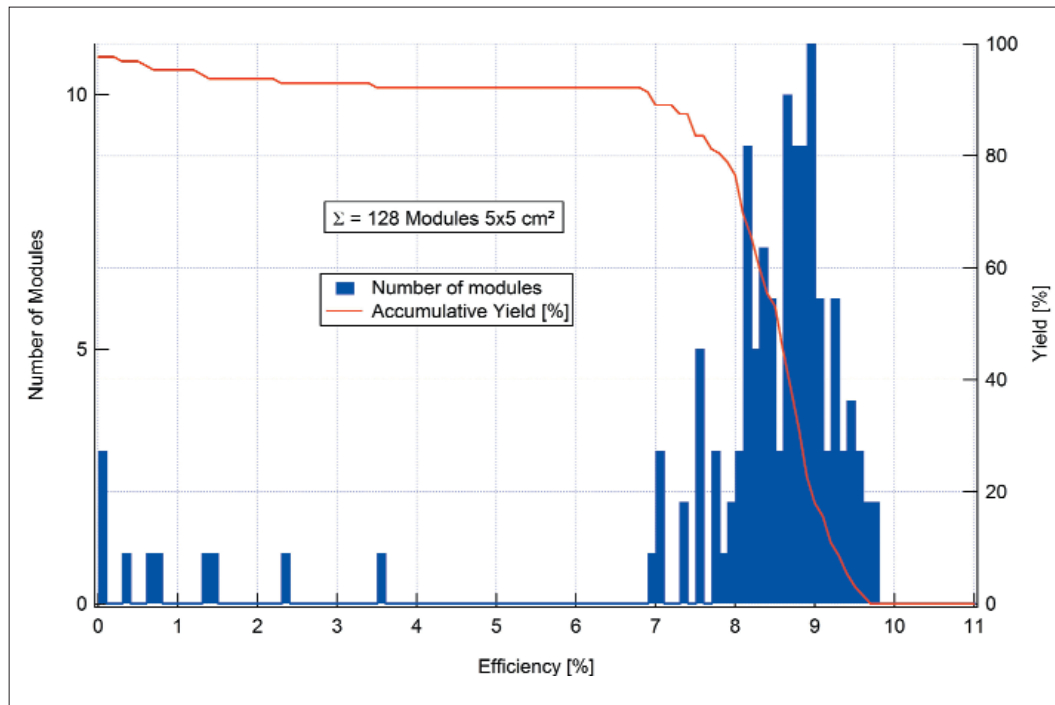


**Fig. 1:** Efficiencies of all baseline modules on  $5 \times 5 \text{ cm}^2$  processed during 6 months July to December 2004. The blue histogram shows the number of modules in an efficiency range of 0.1%, respectively, the red curve shows the accumulative yield.

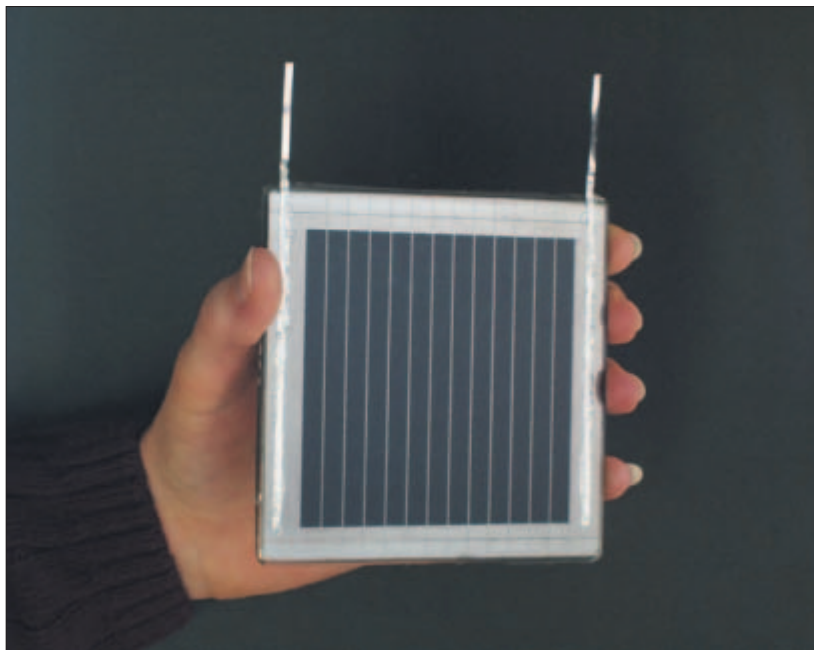


**Fig. 2:** Encapsulated  $\text{CuInS}_2$  module with 13 integrated series connected cells on a  $10 \times 10 \text{ cm}^2$  glass substrate

## Thin film photovoltaics: diagnostics and repair

R. Scheer  
 ■ HMI, SE3

The inherent advantage of thin film photovoltaic modules is the monolithic integration of a large number of solar cells on a substrate. These cells are series interconnected as a result of the production scheme and do not have to be interconnected ex post during module fabrication like in the wafer technology. However, this advantage may turn into a disadvantage if local failures on the substrate of typically  $60 \times 120 \text{ cm}^2$  reduce the overall performance of the thin film module. Failure sources can be inhomogeneous processing along the dimensions of the substrate or simply micro defects due to particles.

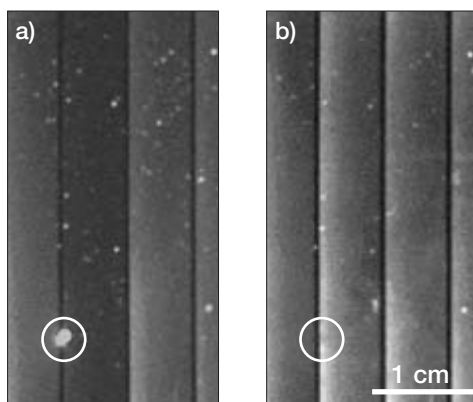


**Fig. 1:** Lock-in infrared thermography images of a  $\text{CuInS}_2$  mini-module from the Hahn-Meitner-Institut baseline, **a)** before and **b)** after module repair. White contrast represents higher temperature due to higher electrical power dissipation. Vertical dark lines depict the positions of the series interconnections. Each grey vertical bar of 0.6 cm width represents one solar cell. White circles mark the position of shunt removal by an excimer laser. Note the reduced brightness of the second left bar in **a)** and its increased brightness after shunt removal.

What is the impact of a local shunt on the module performance? Due to the limited conductance of thin films, a local shunt or weak diode is electrically screened within a distance of typically  $< 1 \text{ cm}$  [1]. If a local shunt, however, is located in the vicinity of the interconnect, the higher conductance of the metallic back electrode leads to a screening length of up to 10 cm. With a total cell length of 120 cm, a single shunt then can deteriorate the photovoltaic action of 20 cm or about 15 % of a cell. If such a shunt occurs on several cells of the module, the power reduction can be in the range of 1 % absolute performance loss.

A local shunt can be visualized by infrared thermography. If an electric current is passed through the module, the shunt represents a position of higher power dissipation and radiates more energy. Higher power dissipation at shunts can also be detected if the electric energy is generated within the module by the photovoltaic effect. This means the module can be put under electrical or light bias in order to record images of infrared response. Figure 1 gives an example of a module under electrical bias. In order to increase the spatial resolution, the lock-in thermography has been used. The left image in **a)** shows the module before repair. Along the interconnect of the second left cell (interconnects represented by vertical dark lines), we find a locally increased temperature due to a strong shunt. The second left cell exhibits a lower brightness in the thermographic image if compared to other cells. The shunt robs the current of the complete second cell during the electric bias as it would rob the current under photovoltaic action. Due to its proximity to the interconnect, the shunt cannot be screened within 1 cm. The current density and thus the thermal radiation of the rest of the second cell is reduced within a distance of 3 cm.

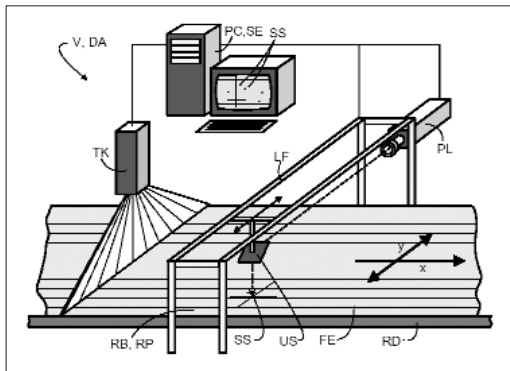


**Fig. 2:** Sketch of a suggested in-line machine for automatic module diagnosis and repair using a Thermocamera (TK) and a laser (PL). The substrate is moving in direction of  $x$ . Due to their higher power dissipation, local shunts (SS) are detected by the thermocamera and recorded by a computer (PC). In case of a local shunt detection, the mirror (US) is positioned above the shunt and a laser pulse is directed onto the module surface at the defected area. The transparent conductive ZnO layer is selectively removed.

Local shunts can be eliminated by local abrasion of all semiconducting layers or by selective removal of the transparent front contact layer. While the former can be accomplished mechanically, we found that by use of an excimer laser, the transparent conductive ZnO layer of a ZnO/CdS/CuInS<sub>2</sub>/Mo stack can be selectively removed. The laser wavelength and the pulse length were 284 nm and 39 ns, respectively. The power threshold for the laser ablation was around 900 mJ/cm<sup>2</sup>. For lower energy density, the ZnO ablation was not complete. A necessary condition for the selective removal of the ZnO layer is the application of only one laser pulse. Under application of a second pulse, the absorber layer is melted leading to new shunt paths. Figure 1b) shows a thermography image of the same module after local shunt removal using the excimer laser. No local heating is observed anymore, the temperature of the second cell due to the passing electrical current is equal to the one of the other cells. Local ablation of the front contact certainly disables the photovoltaic action of the ablated site. Due to the small focus of the laser, however, the site can be small. It is not visible in image b) of

Fig. 1. In the current example, the efficiency of the module rose from 7.71% before shunt removal to 8.42% after shunt removal.

The avoidance of local shunts in a photovoltaic thin film production is a matter of substrate processing and may be accomplished by an improved production equipment. On the other hand, it may be backed up by quality control using larger area IR thermography using modern IR line cameras. We suggested to combine quality control by IR thermography and cell repair by selective laser ablation in an in-line supervision and repair machine [2]. Figure 2 shows a possible set-up for such a diagnosis and repair machine. It provides a shunt statistic which can be used for quality assurance. This piece of equipment in the future may be useful to maintain high yield in photovoltaic thin film production and thereby reduce costs.

- [1] V.G. Karpov, A.D. Compaan, D. Shvydka, *Effects of nonuniformity in thin-film photovoltaics*, Applied Physics Letters, **80** (22), 4256 (2002)
- [2] R. Scheer, *Verfahren und Vorrichtung zu Diagnose und Qualitätssicherung von halbleitenden Dünnschichtsolarmodulen*, Deutsches Patent- und Markenamt, 2004, Anmeldung 10 2004 046 324.7

# Prototype development – flexible high efficiency $\text{Cu(In,Ga)Se}_2$ thin film solar cells for space applications

A. Neisser<sup>1</sup>, C. A. Kaufmann<sup>2</sup>, R. Klenk<sup>2</sup>, R. Scheer<sup>1</sup>, H.-W. Schock<sup>1</sup>

■ 1 HMI, SE3 ■ 2 HMI, SE2

Development of flexible thin film technologies for photovoltaic energy conversion are attracting increasing attention. One of the major driving forces is a growing interest from space industry in lightweight thin film solar arrays of improved power to weight ratio and radiation hardness.

The Dept. SE3 and SE2 of the Hahn-Meitner-Institut, Berlin and Dutch Space B.V., Leiden cooperate in a joint effort with the aim to develop a flexible thin film solar cell based on  $\text{Cu(In,Ga)Se}_2$  (CIGSe) to be integrated into an array structure for space applications. Since late 2003 the cooperation has been supported by the European Space Agency ESA as part of their Thin Film Solar Array Development Program. Furthermore, the Centre for Solar Energy and Hydrogen Research Baden-Württemberg, Stuttgart has joined this collaboration.

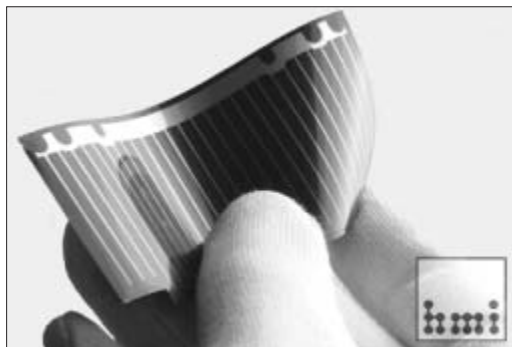


**Fig. 1:** Prototype of a lightweight flexible solar cell based on  $\text{Cu(In,Ga)Se}_2$ . The total area (excluding busbar) is  $27.1 \text{ cm}^2$ . This type of device has reached an efficiency of 15.0% under one-sun reference illumination (AM1.5).

Among the thin film technologies, chalcopyrite based solar cells bear the greatest potential; they have demonstrated energy conversion efficiencies of almost 20% on rigid glass substrates, show excellent radiation hardness in the laboratory as well as in in-flight tests, plus, they have successfully been deposited on flexible substrates. With an apt choice of lightweight material, heavy support structures as they are necessary in current space technologies become obsolete. As a consequence new, lightweight array designs with much higher power to weight ratio can be developed.

Starting point of the space cell development was a standard lab-scale preparation process (baseline) for high efficiency CIGSe thin film solar cells recently established by the Hahn-Meitner-Institut team. The CIGSe thin film devices comprises the layer sequence  $\text{Mo/CIGSe/CdS/i-ZnO/ZnO:Al}$ . Established technologies such as DC-sputtering (Mo), evaporation (NaF, CIGSe, Ni, Al, Au), chemical bath deposition (CdS), and RF-sputtering (i-ZnO, ZnO:Ga) are used. This technology could be successfully transferred to flexible titanium foil substrates without any major loss in cell performance [1]. However, the increase of the solar cell device area from a lab scale area (about  $0.5 \text{ cm}^2$ ) to prototype dimensions necessary for the projected array structure is not straightforward. Therefore, recent efforts have been focused on advances in performance optimization of large area single solar cells (Fig. 1), produced on Ti-foil substrates with an area of up to  $29.7 \text{ cm}^2$  (total area w/o busbar  $27.1 \text{ cm}^2$ ) [2]. First devices showed very low fill factors and process reproducibility was poor. Device analysis revealed that the decrease in device performance was mainly due to parasitic leakage currents shunting the junction. Using lock-in thermography imaging these shunts could be assigned to local defects of the device structure caused by substrate irregularities. Hence a substrate pre-treatment step was introduced and as a result the homo-

geneity and reproducibility of the produced large area devices has been improved. Figure 2 shows a histogram of the number of finished  $27.1 \text{ cm}^2$  samples versus their respective AM1.5 efficiency over a period of two months. The high reproducibility of the Hahn-Meitner-Institut baseline as illustrated by a narrow distribution around 12%–13% is an important prerequisite for the ongoing array development at Dutch Space. Current record efficiencies for a  $27.1 \text{ cm}^2$  CIGSe thin film device are 15.0% under AM1.5. This represent the highest values so far reported for a large area thin film single solar cell. However, there is still a significant drop in device performance (particularly the fill factor) with increased area (see Table 1). Large area devices reach only 85%–90% of the performance of small ones. Ongoing process development large and the analysis of a large number of samples have shown that there are three main contributions to the observed scale-up loss:

- grid finger losses
- parasitic leakage currents – local shunts
- lateral inhomogeneities of device parameters due to material non-uniformities

About 8% of the observed scale-up loss is due to the higher grid finger losses caused by the much higher current transported by each grid finger in the large area cell compared to small area record devices. The impact of local defects on cell performance could be reduced to less than 3% of the total power generated by the device as  $j(V)$  curve analysis of 37 prototype devices revealed. This was mainly due to the substrate pre-treatment optimization which resulted in a highly reduced number of local shunts. The remaining scale-up loss we attribute to lateral non-uniformities of the absorber layer composition of the cell. Indications for such non-uniformities have been obtained by laterally resolved spectral response measurements and by thermography. Studies of arrays of small area test cells on a  $8 \times 4 \text{ cm}^2$  substrates are underway in order to quantify this effect.

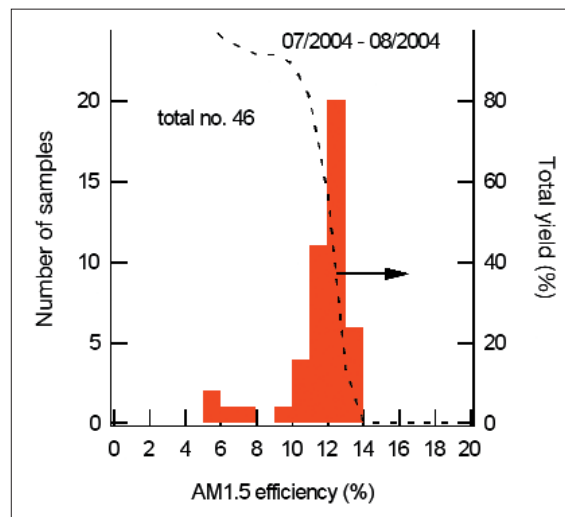


**Fig. 2:** Distribution of AM1.5 efficiencies of all processed  $27.1 \text{ cm}^2$  devices of the Hahn-Meitner-Institut baseline over a period of two month. The narrow distribution reflects the high level of process reproducibility of the baseline process for flexible solar cells. The dashed line depicts the number of samples above a respective efficiency threshold value.

area [cm <sup>2</sup> ]	$V_{oc}$ [mV]	$j_{sc}$ [ $\frac{\text{mA}}{\text{cm}^2}$ ]	ff [%]	$\eta$ [%]
27.1	640	33.93	69.3	<b>15.0</b>
0.5	640	34.48	75.6	<b>16.7</b>

**Table 1:** Device parameters of best large area device ( $27.1 \text{ cm}^2$ ) on titanium foil under AM1.5 illumination ( $100 \text{ mW/cm}^2$ ). Parameters for a small area reference cell are included for comparison.

- [1] C. A. Kaufmann, A. Neisser, R. Klenk, R. Scheer, *Transfer of Cu(In,Ga)Se<sub>2</sub> thin film solar cells to flexible substrates using an in situ process control*, Thin Solid Films in press (2004)
- [2] A. Neisser, C. A. Kaufmann, R. Klenk, R. Scheer, M. A. Kroon, G. Oomen, H.-W. Schock, *Prototype Development – Flexible Cu(In,Ga)Se<sub>2</sub> Thin Film Solar Cells for Space Applications*, Proc. of 31<sup>st</sup> IEEE PVSC, Florida, 2005, accepted for publication

**Corresponding author:**

A. Neisser  
axel.neisser@hmi.de

# Hot electrons at the interface of p-InP

M. Neges, K. Schwarzburg, F. Willig

■ HMI, SE4

The theoretical limit for the efficiency of a photovoltaic converter operated under non-concentrated sunlight is 67%, whereas the limit of a single band gap solar cell is around 30% [1]. Conventional single junction solar cells simply cannot use the excess kinetic energy of those charge carriers created by the absorption of photons with energy greater than the band gap. Present physical models for solar cells ignore effects due to hot charge carriers and assume that all photo-generated carriers thermalize to the temperature of the crystal lattice prior to charge transport via diffusion and drift. However, if the thickness of the light-absorbing layer becomes smaller, this assumption is no longer valid. There is even the suggestion in the literature that a single band gap solar cell can approach the general efficiency limit of 67% [2] if all the hot carriers can be collected at an appropriate contact.

To obtain somewhat more quantitative data concerning dynamics of hot charge carriers at room temperature at low excess carrier densities, we carried out Monte Carlo simulations on *p*-type InP. The latter was selected as the model system, since relevant material parameters are available in the literature. Because of the small electron-hole effective mass ratio and the fast scattering rates for holes in *p*-type material, our modeling was restricted to the photo-generated electrons. Scattering with LO-phonons, acoustic phonons (deformation potential and piezoelectric), charged impurities, and holes was included in the model. Two geometries were considered for the light-absorbing layer. Firstly, a semi infinite half-space where the boundary acted as an ideal electron-collecting interface. This scenario (*bulk*) mimics the electrically neutral absorbing layer, comprising typically the whole wafer of a conventional pn-junction solar cell. The second structure (*slab*) was a 50 nm thin slab of InP:Zn, where the front and the back

side contacts were the electron collectors. This scenario is an approximation for a solar cell structure with several thin layers stacked or a cell consisting of large nm particles. Figure 1 shows the electron energy distribution for the *bulk* structure. The electron generation depth (10, 75, 750 nm) was varied and also the doping level (a:  $N_A = 5E17 \text{ cm}^{-3}$ , b and c:  $N_A = 2E14 \text{ cm}^{-3}$ , c with reduced LO-phonon scattering rate). From Fig. 1 it is evident, that the electron energy distribution is non-thermal even at room temperature unless the electrons are generated far away (750 nm) from the interface combined with a medium doping level. Thus, it is not possible to describe the actual energy distribution as a Maxwell-Boltzmann distribution at an elevated temperature. As can be expected, the deviations become the stronger the lower the electron-hole scattering rates (a→c). Figure 2 presents an analysis of the possible gain in energy conversion under different conditions. It shows the normalized energy flux at the interface under solar illumination conditions. The energy loss of hot electrons is small for the 50 nm thick *slab* structure, while the *bulk* absorber would be a bad hot-electron converter. In summary, the simulations demonstrate that hot carrier dynamics are important at the contact even at room temperature. The actual energy distribution of hot electrons must be determined using parameters characteristic for the specific material. It cannot be approximated by a thermal distribution at a high temperature. Hot carrier collection can become important in future generations of photovoltaic devices that incorporate thin layers or aim at utilizing hot carriers directly.

- 
- [1] P. Würfel, T. Trupke, *Physik Journal* **2**, 45–51 (2003)  
 [2] R. T. Ross, A. J. Nozik, *J. Appl. Phys.* **53**, 3813–3818 (1982)

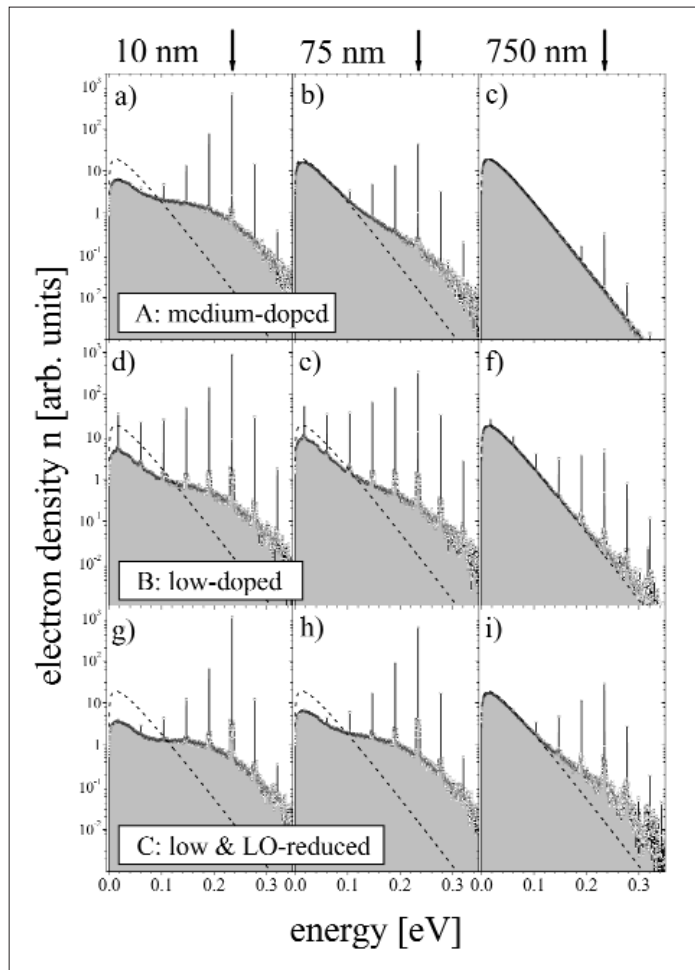


**Fig. 1:** Simulated energy distributions of the electron density in bulk-type InP:Zn at 300 K for electrons with generation depths of 10 nm (left), 75 nm (middle) and 750 nm (right). Each row corresponds to different material parameters (see text). The excitation energy is 234 meV above the conduction band minimum and is indicated by the arrows on top. Dotted lines show the corresponding Maxwell-Boltzmann distribution.

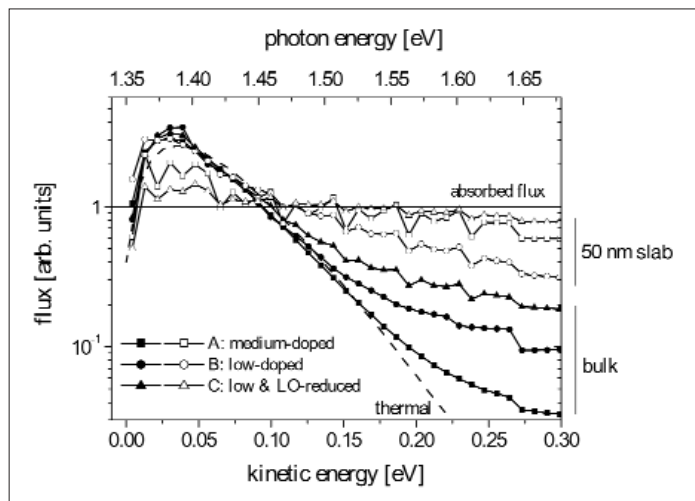


**Fig. 2:** Energy distribution of the total electron flux at the contact for the *bulk* scenario (closed symbols) and for a slab, 50 nm thick (open symbols). The distributions are normalized to the absorbed photon flux. The photon source was modeled as a black body with  $T=5800$  K. For comparison also a thermal distribution is depicted.

# Ultrafast electron dynamics measured with femtosecond two-photon photoemission

L. Gundlach<sup>1</sup>, R. Ernstorfer<sup>1</sup>, E. Riedle<sup>2</sup>, R. Eichberger<sup>1</sup>, F. Willig<sup>1</sup>

■ 1 HMI, SE4 ■ 2 Biomolekulare Optik, LMU München

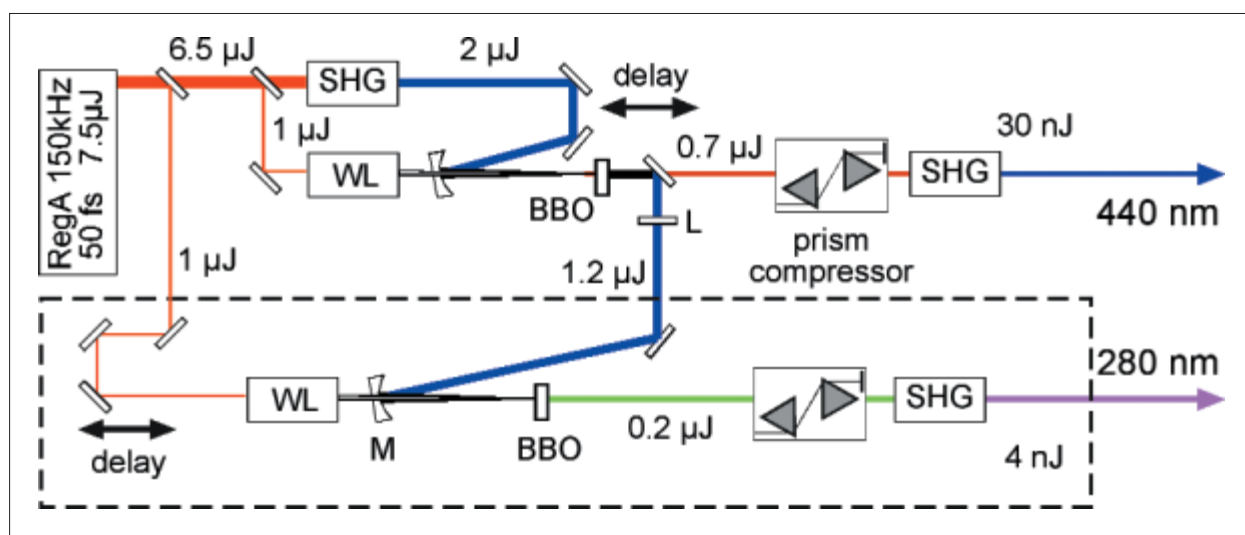


**Fig. 1:** Setup for two 150 kHz NOPAs pumped with one 400 nm SHG pulse (light blue). The second NOPA is shown inside the dashed box. The crosscorrelation of the output pulses is sub-30 fs.

Time-resolved two-photon photoemission (TR-2PPE) is the method of choice for investigating ultrafast photo-driven interfacial processes in the time domain, provided the respective interface can be exposed to ultrahigh-vacuum [1, 2]. The TR-2PPE measurement collects simultaneously information on the energy distribution of the photo-generated electrons and the time evolution of the intermediate state population near the interface. The 2PPE method offers unequalled sensitivity when compared with other pump-probe techniques, e.g. transient absorption, since the photoemitted electrons are counted directly by the detector. Hitherto, two different types of laser sources were employed for 2PPE measurements. On the one hand high repetition rate laser sources, i.e. systems operating at 100 kHz to MHz repetition rate were used, that deliver fairly long pulses with often limited wavelength tunability based on optical parametric amplification (OPA) for frequency tuning or harmonic generation. On the other hand low repetition rate laser sources with repetition rates up to 1 kHz and with a large number of photons per

pump pulse were employed. The latter systems allow only for slow signal accumulation, the superior noncollinear optical parametric amplification (NOPA) technology [3] can provide, however, extremely short and highly tunable pulses. Recently, tunable sub-20 fs ultraviolet pulses have been achieved with appropriate chirp management in the visible [4]. We report here on a significant improvement of the laser source for 2PPE measurements by adapting the NOPA scheme to operation at 150 kHz repetition rate. Furthermore, a second NOPA was operated simultaneously with one common pump system by utilizing the 400 nm pump pulse for the first NOPA again also in the second NOPA. This way two independently tunable ultrafast light sources are available (Fig. 1).

The improved tunability and shorter duration of the two laser pulses were tested in 2PPE measurements probing the lifetime of image potential states at Cu(111) and Ag(111) surfaces. Image potential states at metal surfaces have been studied extensively before [5]. The low-index surfaces of noble-metals exhibit a surface-projected bandgap centered at  $\Gamma$  (Fig. 2). An electron in front of such a surface is trapped by the induced image potential on one side and the bandgap on the other side. The resulting potential generates a Rydberg-like series of bound states in the direction of the surface normal. These states can be optically populated from the occupied surface state (SS) either resonantly or off-resonantly via quasi-elastic scattering. The main decay channel for the excited image potential state (IS) is governed by the overlap of the IS with the bulk. Earlier TR-2PPE studies by Schönlein et al. have proposed lifetimes of less than 20 fs for the  $n=1$  and  $n=2$  IS of Ag(111), respectively [6]. More recently, Lingle et al. have reported  $32 \pm 10$  and sub-20 fs for the  $n=1$  and  $n=2$  IS of the same

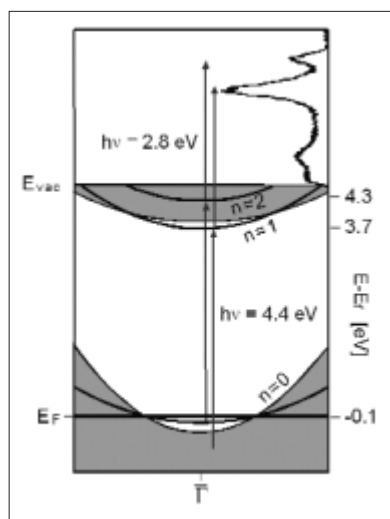


**Fig. 2:** Surface projected bulk band structure and dispersion of the  $n=0$  surface state,  $n=1$  and  $n=2$  image potential state together with the TR-2PPE scheme for the Ag(111) surface. Effective electron masses and binding energies taken are from literature. The arrows indicate direct excitation from the  $n=0$  surface state to the  $n=2$  image potential state and indirect excitation from bulk states to the  $n=1$  image potential state with photons  $h\nu=4.4\text{ eV}$ . The second pulse ( $h\nu=2.8\text{ eV}$ ) generates the depicted kinetic energy spectrum of the photoemitted electrons.

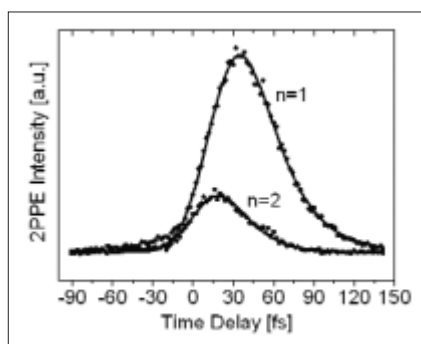


**Fig. 3:** Transient 2PPE signal for the  $n=1$  and  $n=2$  image potential state at Ag(111) together with the fitted curves obtained from the Bloch model. The lifetimes are  $25 \pm 2$  fs and  $18 \pm 2$  fs for the  $n=1$  and  $n=2$  image potential state, respectively.

system, respectively [7]. The pulse durations in the above experiments were up to six times longer than the reported lifetimes. The values had been extracted from the measurements by fitting the data with optical Bloch equations. This method relies on the exact knowledge of time zero, i.e. the time of maximum overlap between pump and probe pulse. With the improved laser setup described here, it was possible to obtain the IS lifetimes directly from the clear deviations of the measured signals from the crosscorrelation trace and to extract time constants as short as 12 fs by means of optical Bloch equations, as well as by fitting with a simple rate model (Fig. 3). The time scale of the thus measured lifetimes is in good agreement with values deduced earlier by other groups.

- [1] R. Haight, Surf. Sci. Rep. **21**, 275 (1995)
- [2] L. Töben, L. Gundlach, T. Hannappel, R. Ernstorfer, R. Eichberger, F. Willig, Appl. Phys. A **78**, 239 (2004)
- [3] G. Cerullo, M. Nisoli, S. De Silvestri, Appl. Phys. Lett. **71**, 3616 (1997)
- [4] P. Baum, S. Lochbrunner, E. Riedle, Appl. Phys. B **79**, 1027 (2004)
- [5] P. Echenique, R. Berndt, E. Chulkova, T. Fauster, A. Goldmane, U. Höfer, Surf. Sci. Rep. **52**, 219 (2004)
- [6] R. W. Schönlein, J. G. Fujimoto, G. L. Eesley, T. W. Capehart, Phys. Rev. B **43**, 4688 (1991)
- [7] J. R. L. Lingle, N.-H. Ge, R. E. Jordan, J. D. McNeill, C. B. Harris, Chem. Phys. **205**, 191 (1996)

#### Corresponding author:

L. Gundlach  
gundlach@hmi.de

# Improved structure and performance of the InP/GaAsSb interface in a resonance tunneling diode

Z. Kollonitsch<sup>1</sup>, H.-J. Schimper<sup>1</sup>, U. Seidel<sup>1</sup>, K. Möller<sup>1</sup>, S. Neumann<sup>2</sup>, F.J. Tegude<sup>2</sup>, T. Hannappel<sup>1</sup>, F. Willig<sup>1</sup>  
 ■ 1 HMI, SE4 ■ 2 University Duisburg-Essen, Solid-State Electronics Department, Duisburg, Germany

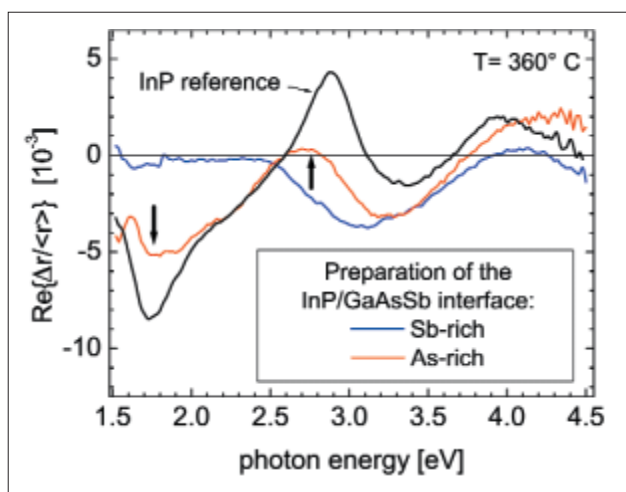


**Fig. 1:** Reflectance anisotropy (RA) spectra after InP was grown for 5 s (20–25 Å) on GaAsSb. The blue curve corresponds to InP growth on the Sb-rich GaAsSb(100)–(1×3) reconstruction, and the red curve to InP growth on the As-rich GaAsSb(100)–c(4×4) reconstruction. The black curve shows for comparison the spectrum of a homoepitaxially grown P-rich InP(100) surface.

A main challenge of metalorganic vapor phase epitaxy (MOVPE) and molecular beam epitaxy (MBE) process control is the improvement of III–V heterointerfaces. The InP/GaAsSb heterocontact is of interest for electronic devices based on the lattice constant of InP, e.g. multijunction solar cells, double heterojunction bipolar transistors, and resonance tunneling diodes (RTDs). Interfaces between an antimony (Sb) containing layer and a subsequent layer without Sb are known to suffer from Sb segregation [1]. It is still under investigation, how to reduce interdiffusion at the interfaces but most researchers would agree that control over the surface reconstruction of the Sb containing layer is a promising approach to reduce the Sb segregation. In a previous study on InAs/GaInSb heterointerfaces [1] Sb segregation was found quantitatively linked to the group V stoichiometry of the GaInSb surface reconstruction that served as the template for interface formation. Growth of InP on two different reconstructions of the GaAsSb(100) surface was investigated here, namely the Sb-rich (1×3) reconstruction and the As-rich c(4×4) reconstruction [2]. In the following the growth of InP on the Sb-rich (As-rich) GaAsSb(100) surface will be referred to as Sb-rich (As-rich) interface preparation.

The samples were prepared in an MOVPE reactor equipped with a patented exit for sample transfer into an ultrahigh vacuum (UHV) chamber [3]. The growth of the InP/GaAsSb heterointerface was monitored in the MOVPE environment with reflectance anisotropy/difference (RA/RD) spectroscopy. After transfer of the sample to UHV photoelectron spectroscopy (UPS/XPS) and low energy electron diffraction (LEED) were performed. The blue curve in Fig. 1 shows the in-situ RA spectrum after InP was grown for 5 s on the Sb-rich GaAsSb(100)–(1×3) reconstruction.

The RA spectrum is obviously very different from the reference RA spectrum of a homoepitaxially grown P-rich InP(100) surface (black curve). XPS and UPS measurements (not shown here) indicated that the group V elements intermix at the interface. The red curve in Fig. 1 shows the in-situ RA spectrum after InP was grown for 5 s on the As-rich GaAsSb(100)-c(4×4) reconstruction. Clearly, the red curve in Fig. 1 is much more similar to the black curve than the blue curve. This fact is attributed to the reduction in the interfacial diffusion of Sb. The peak at around 1.7 eV indicates that P-dimers are formed on the surface of InP [4]. The incomplete peak of the red curve at around 2.8 eV indicates intermixture of group V atoms in the second and third layer at the interface [4]. In conclusion, the As-rich preparation of the interface leads to an improved InP layer growth on GaAsSb compared to the Sb-rich preparation of the interface.

RTDs were prepared (upper panel in Fig. 2) in order to compare the electronic behavior of the Sb-rich and As-rich interface preparations. The preparation of the two RTDs was identical except for the Sb- versus As-rich termination of GaAsSb. The functionality of *p*-type RTDs is based on quantum mechanical tunneling of charge carriers through a double barrier in the valence band [5]. Each InP-barrier had a thickness of 7 nm. The nonlinear current-voltage (*I*-*V*) characteristic is sensitive to the quality of the interfacial layers. The *I*-*V* characteristics of the RTD with the differently prepared interface display the symmetry with respect to the sign of the voltage (center and lower panel in Fig. 2). Non-symmetric *I*-*V* curves are attributed to poor interfacial layers. Clearly, the RTD with the As-rich prepared interface showed a more symmetric *I*-*V* characteristic than that with the Sb-rich interface.

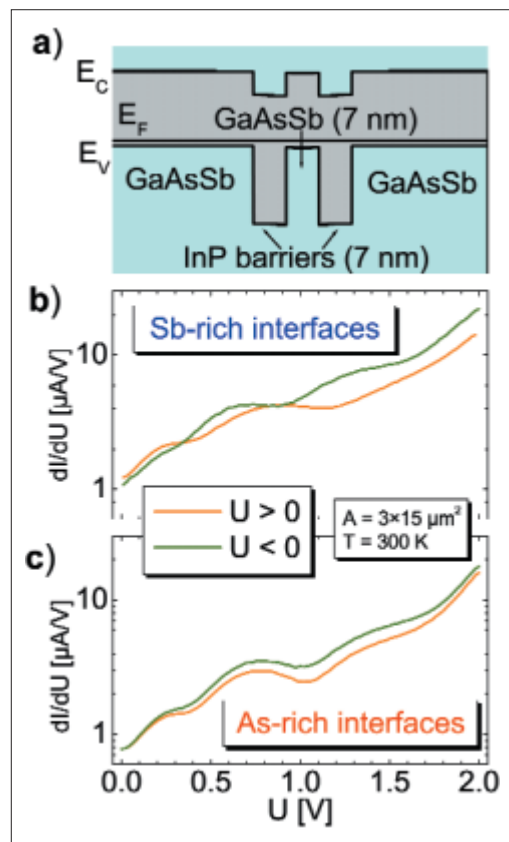


**Fig. 2:** a) Band diagram of the active region of the InP/GaAsSb *p*-type RTD. b) Non-symmetric *I*-*V* curves for the RTD with the Sb-rich InP/GaAsSb interfaces. c) Less non-symmetric *I*-*V* curves for the RTD with the As-rich InP/GaAsSb interfaces.

- [1] J. Steinshnider, J. Harper, M. Weimer, C.-H. Lin, S. S. Pei, D. H. Chow, *Phys. Rev. Lett.* **85**, 4562 (2000)
- [2] Z. Kollonitsch, K. Moller, F. Willig, T. Hannappel, *J. Cryst. Growth* **272**, 694 (2004)
- [3] T. Hannappel, S. Visbeck, L. Töben, F. Willig, *Rev. Sci. Instrum.* **75**, 1297 (2004)
- [4] C. Castillo, B. S. Mendoza, W. G. Schmidt, P. H. Hahn, F. Bechstedt, *Phys. Rev. B* **68**, 041310(R) (2003)
- [5] J. F. Lampin, F. Mollot, *Appl. Phys. Lett.* **71**, 1080 (1997)

**Corresponding author:**  
Z. Kollonitsch  
kollonitsch@hmi.de

# Reactive magnetron sputtering of $\text{CuInS}_2$ : a new prospective deposition method for thin film solar cells?

T. Unold, K. Ellmer

■ HMI, SE5

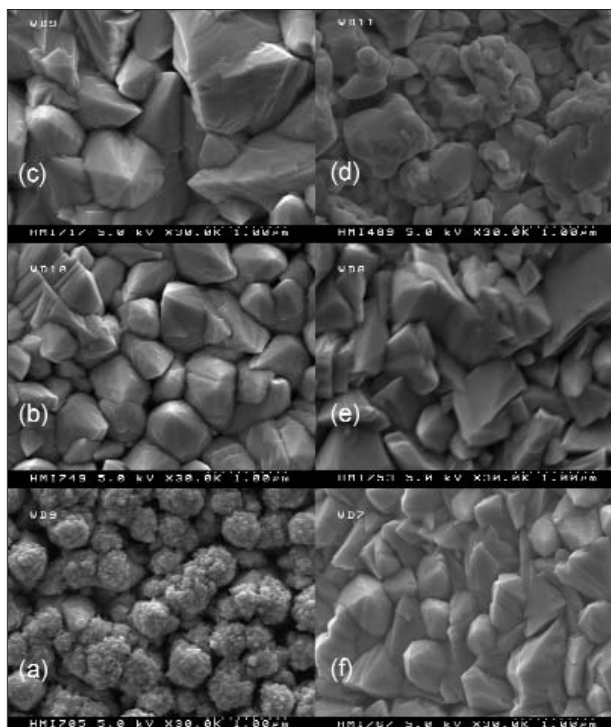


**Fig. 1:** REM images of  $\text{CuInS}_2$  films prepared by reactive magnetron sputtering at different temperatures  $T_s$  and different  $\text{Cu/In}$  ratios  $r$ . **a)**  $T_s=350^\circ\text{C}$ ,  $r=1.1$  **b)**  $T_s=420^\circ\text{C}$ ,  $r=1.1$  **c)**  $T_s=500^\circ\text{C}$ ,  $r=1.1$  **d)**  $r=2.3$ ,  $T_s=500^\circ\text{C}$  **e)**  $r=1.0$ ,  $T_s=500^\circ\text{C}$  **f)**  $r=0.9$ ,  $T_s=500^\circ\text{C}$

Thin-film chalcopyrite solar cells are usually prepared by coevaporation or by a sequential process consisting of sputtering of the metal precursors followed by a sulfurization or selenization and recrystallization step at about  $500^\circ\text{C}$  [1]. For a large-scale production of thin-film solar cells a direct one-step deposition process of the absorber layer would be advantageous, allowing for an in-line deposition of all solar cell layers [2]. Magnetron sputtering is a well established deposition method, which allows for low temperature thin film growth on large areas. In fact, millions of square meters per year of architectural glass are being coated using magnetron sputtering at the present.

So far there have been very few studies investigating the deposition of electronic device-quality semiconductor materials by magnetron sputtering. Because of the sensitivity of electronic devices to even small (ppm) amounts of defects the requirements for the sputtering process in this case are much more stringent than in the case of optical coatings, where the main requirement is uniformity. In particular, the presence of high energy ions in the sputtering plasma pose a difficult challenge, since they may create structural and electronic defects in the growing film.

We have deposited  $\text{CuInS}_2$  absorber layers by reactive magnetron sputtering from metallic copper and indium targets in an  $\text{Ar-H}_2\text{S}$  atmosphere. In order to optimize the reactive sputtering process for our films, the substrate temperature,  $\text{H}_2\text{S-Ar}$  ratio and  $\text{Cu/In}$  ratio have been systematically varied. The structural, optical as well as the solar cell properties were analysed by Raman spectroscopy, photoluminescence, Scanning Electron Microscopy (SEM), current-voltage and quantum efficiency measurements.

In Fig.1 we show SEM images for films sputtered at 3 different substrate temperatures,  $T_s$ , and three different  $\text{Cu/In}$  ratios ranging from  $0.9 \leq \text{Cu/In} \leq 2.3$ . For the films with  $r = \text{Cu/In} \sim 1.1$  the film morphology changes considerably when the substrate temperature is raised from  $350^\circ\text{C}$  to  $500^\circ\text{C}$ . Whereas the film deposited at low temperature is very porous and *cereals-like*, the films become more dense and of columnar morphology at higher temperatures. Typical grain sizes evolve from about  $350\text{ nm}$  at  $420^\circ\text{C}$  to about  $1\text{ micrometer}$  at  $500^\circ\text{C}$ . Similarly for films grown at  $T_s=500^\circ\text{C}$ , the films become increasingly more dense with decreasing  $\text{Cu/In}$  ratio. This change in morphology is accompanied by a change in the structural phases present in the film as seen in the Raman spectra shown in Fig.2. The film grown at  $350^\circ\text{C}$ , shows very broad spectral features and in particular a strong signal due to the  $\text{CuIn}_3\text{S}_8$  phase at  $340\text{ cm}^{-1}$  which is found not to be helpful for

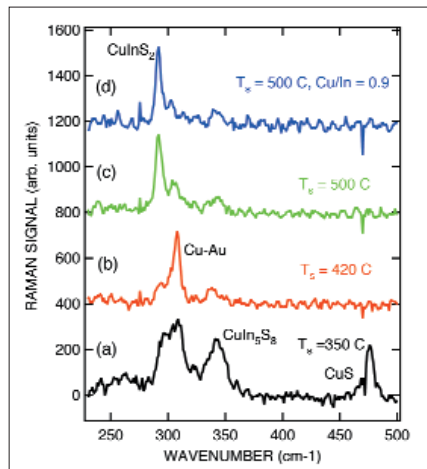


**Fig. 2:** Raman spectra for three copper rich films and one indium-rich film.

**a)**  $T_s = 350^\circ\text{C}$ ,  $r = 1.1$  **b)**  $T_s = 420^\circ\text{C}$ ,  $r = 1.1$   
**c)**  $T_s = 500^\circ\text{C}$ ,  $r = 1.1$  **d)**  $r \sim 0.9$ ,  $T_s = 500^\circ\text{C}$

good solar cell performance. The film grown at  $420^\circ\text{C}$  shows a dominant  $\text{CuInS}_2$  resonance around  $300\text{ cm}^{-1}$ , however not the one corresponding to the chalcopyrite ordering, but rather to a Cu-Au defect ordering [3]. In previous work this defect ordering has been correlated with a deteriorated solar cell performance. The spectrum for the film grown at  $500^\circ\text{C}$  is dominated by the chalcopyrite resonance at  $294\text{ cm}^{-1}$  with only small amounts of the defect ordering phase noticeable. These three films have been grown with a  $\text{Cu/In} \sim 1.1$  (corresponding to Fig. 1a–c). On the top of the graph we show an indium-rich deposited film ( $\text{Cu/In} \sim 0.9$ ,  $T_s = 500^\circ\text{C}$ ). It can be seen that now the chalcopyrite mode is even a bit more pronounced. This result has been surprising considering previous results obtained for coevaporated and sequentially processed films, where  $\text{Cu/In} \leq 1$  always led to an increased defect ordering. The fact that we observe the opposite points to some fundamental differences in the reactive sputtering growth process compared to the evaporation process. Stoichiometric or indium-rich deposition of  $\text{CuInS}_2$  absorber layers would be desirable because it would eliminate the need for the KCN etching step currently used to remove the CuS surface layer present on copper-rich films.

We have also measured the photoluminescence properties of our films to get an estimate of the electronic quality of the reactively sputtered absorber layers. The photoluminescence measurements revealed level spectra very similar to the spectra found for films from the standard sequential and coevaporation processes. This indicates that the presence of ion bombard-

ment in the reactive sputtering process does not introduce fundamental qualitative changes to the defect structure of the films.

Solar cell devices have been produced from our optimized absorber layers, utilizing the Hahn-Meitner-Institut baseline processes consisting of a KCN etching step, a chemical bath deposition of the CdS buffer layer and magnetron sputtering of the ZnO top contact. The results for our best cell are presented in Fig. 3 showing an efficiency of  $\eta = 8.8\%$ , a short circuit current of  $23\text{ mA}$  and an open-circuit voltage of  $650\text{ meV}$ . Although this efficiency is still somewhat lower than the best efficiencies found for the sequential and the coevaporation processes ( $\eta \sim 12\%$ ), it is nevertheless a promising step toward the goal of a solar cell exclusively prepared by sputtering processes. In our study we have not identified principle obstacles to the magnetron sputtering deposition of device-quality semiconducting films. Rather, the directly sputtered absorber films seem to show an improved film morphology, consisting of columnar grains without large voids and a relatively smooth surface. At the moment the efficiency of our devices is mainly limited by the open-circuit voltage of approximately  $650\text{ meV}$ . We think that this is due to defects at the  $\text{CuInS}_2/\text{CdS}$  hetero-interface, possibly caused by ion bombardment in the sputtering process. We are currently investigating further optimizations and changes to the magnetron sputtering process to overcome this limitation.

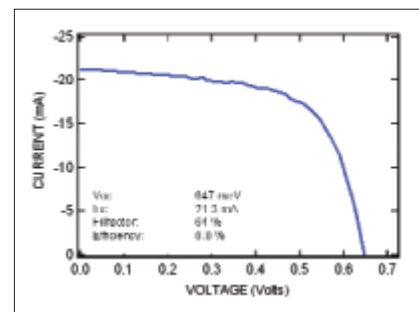


**Fig. 3:** AM1.5 illuminated current voltage characteristic for a ZnO/CdS/CuInS<sub>2</sub>/Mo solar cell prepared by reactive sputtering,  $T_s = 500^\circ\text{C}$ ,  $r \sim 1.1$ .

- [1] J. Klaer, *et al.*, *Efficient CuInS<sub>2</sub> Thin Film Solar Cells Prepared by a Sequential Process*, *Semicond. Sci. Tech.* **13**, 1456 (1998)
- [2] T. Unold, J. Hinze, K. Ellmer, *CuInS<sub>2</sub> Absorber Layers and Solar Cells Deposited by Reactive Magnetron Sputtering from Metallic Targets*, 19<sup>th</sup> Europ. Photovolt. Sol. En. Conf. (2004) Paris, 1917
- [3] J. Alvarez-García *et al.*, *Raman scattering structural evaluation of CuInS<sub>2</sub> thin films*, *Thin Solid Films* **387**, 216 (2001)

**Corresponding author:**

T. Unold  
 unold@hmi.de

# Surface passivation of MoS<sub>2</sub> or WSe<sub>2</sub> for optimised photoconversion efficiencies

T. Moehl, H. Tributsch

■ HMI, SE5

Photoelectrochemical microwave reflectivity measurements offer a deep insight into the interface between semiconductor and electrolyte. In addition to the light induced excess charge carriers that reach the external circuit and are detected via the photocurrent the microwave reflection simultaneously provides information about the photo-induced excess charge carriers which remain in the semiconductor. In this way it is possible to directly observe the influence of surface changes on the excess charge carriers at the interface and thus on photovoltaic quality [1].

The aim of this project is the passivation of surface states in layered type semiconductors like molybdenum disulfide (MoS<sub>2</sub>) or tungsten diselenide (WSe<sub>2</sub>). These compounds exhibit promising characteristics for the application in thin film solar cells [2]. They have high adsorption coefficients (up to  $3 \cdot 10^5 \text{ cm}^{-1}$ ) with energy gaps of 1,2 to 1,7 eV. Single crystals of WSe<sub>2</sub> gave energy conversion efficiencies of 17% in wet iodine-iodide solar cells [3]. The crystal structure is strongly anisotropic revealing a chemical inert van der Waals surface perpendicular to the c-axis and a highly reactive surface consisting of unsaturated bonds parallel to the c-axis (Fig. 1). Like graphite these crystals have electronically and chemically diverse attributes depending on which surface is investigated.

The unsaturated bonds of molybdenum are held responsible for unfavoured side reaction of charge carriers. The first steps of (photo)corrosion of these crystals in aqueous electrolyte is starting at those and the recombination of light induced excess charge carriers is mainly taking place at unsaturated bonds at the crystal edges. In order to develop solar cells based on these compounds, single or polycrystalline, understanding of the behaviour of the unsaturated bonds at the crystal edges is necessary.

Tween 80 and related compounds possess a long aliphatic side chain at a sorbitol ring. The other alcoholic groups of the condensed Hexose are substituted by poly-oxo-ethylenic groups. This molecule intercalates with its hydrophobic group in between the van der Waals layers (which could be demonstrated by XRD) and the polar oxo groups interact with the unsaturated bonds at the crystal edges (Fig. 1). The effect of the modification could be clearly detected in the change of the photocurrent and the microwave reflection (Fig. 2).

Figure 2 shows the enhancement of the photocurrent (solid line) after the modification with Tween 80, which also starts at a lower potential vs. SCE (Saturated Calomel Electrode) because of the suppressed surface recombination. This is supported by the measured microwave reflection (dashed line) which indicates lower surface recombination by an earlier rise of the signal after the adsorption of Tween 80 ( $\Delta V \approx 100 \text{ mV}$ ) and more accumulated excess charge carriers in the range of the steady state photocurrent ( $V > 700 \text{ mV}$ ). The results show that Tween 80 blocks the adsorption sites for water and reduces the surface states induced by the dangling bonds.

On the way to polycrystalline solar cells out of MoS<sub>2</sub> and related layered compounds the understanding of the interaction of different functional groups of adsorbates with the crystal edges has to be understood. The impact of adsorbates on corrosion, recombination and charge transfer can be tested and studied by the simultaneous measurement of photocurrent and microwave reflection.

- 
- [1] G. Schlichthorl, H. J. Lewerenz, *Journal of Electroanalytical Chemistry* **443**, 9–31 (1998)
- [2] *Photoelectrochemistry and Photovoltaics of Layered Semiconductors*; edited by A. Aruchamy; Kluwer Academic Publishers (Dordrecht, 1992)
- [3] O. N. Srivastava, G. Prasad, *J. Phys. D: Appl. Phys.* **21**, 1028–1030 (1988)

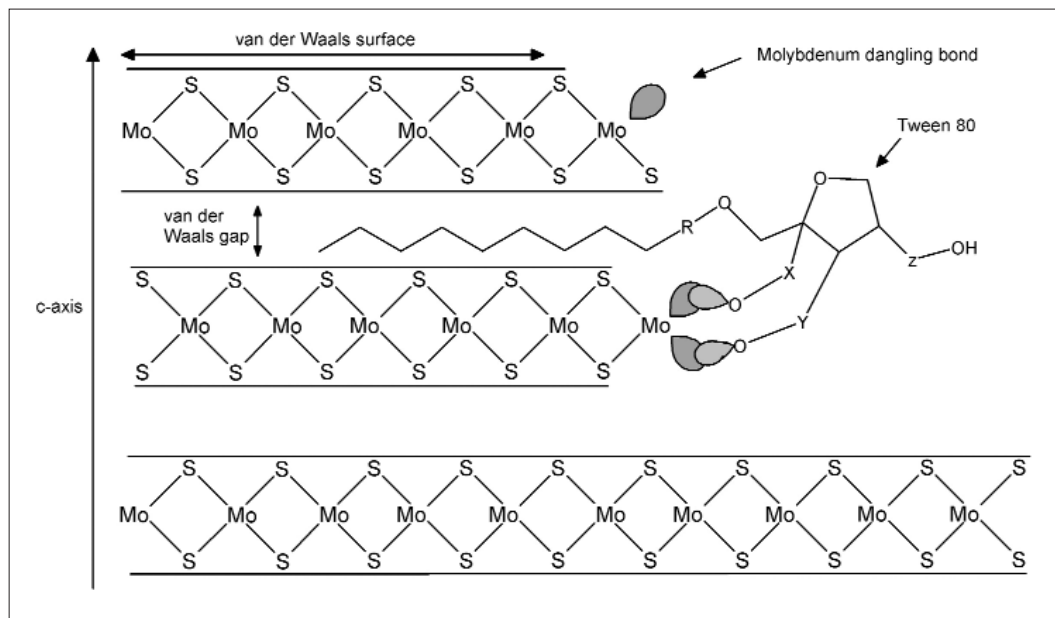


**Fig. 1:** Schematic figure of the different crystal surfaces in MoS<sub>2</sub> and possible adsorption mechanism of Tween 80 and related compounds (X, Y and Z are side chains of the  $-(O-CH_2-CH_2)-$  type with different lengths).

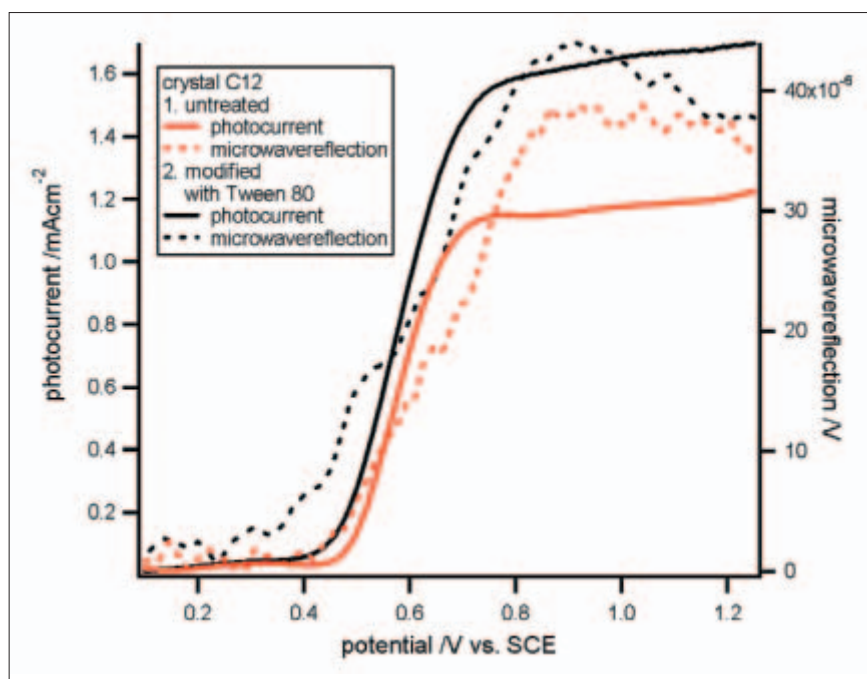


**Fig. 2:** MoS<sub>2</sub> (crystal charge c12) before and after the modification with Tween 80 (5 wt% aqueous solution for 15 h) under 8,7 mW/cm<sup>2</sup> halogen illumination in 0,5 M K<sub>2</sub>SO<sub>4</sub> with 0,2 M K<sub>3</sub>/K<sub>4</sub>[Fe(CN)<sub>6</sub>] and 20 mV/s cycle speed.

# Polymer electrolyte membrane (PEM) fuel cells: new catalysts and bionic aspects

H. Tributsch, S. Fiechter, P. Bogdanoff

■ HMI, SE5

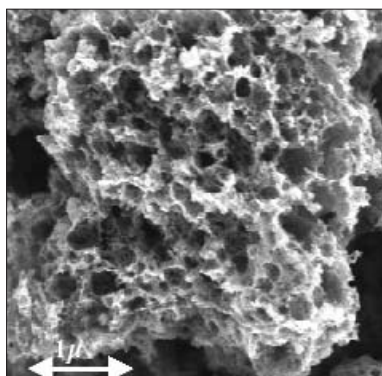


**Fig. 1:** Sponge-like catalyst prepared by pyrolysis of a cobalt porphyrin in the presence of iron oxalate.

## Nature's regenerative strategy: Examples for bionic research.

Nature's regenerative strategy can be considered as a close example for a sustainable energy supply in a future industrial society. Striking natural phenomena are the light induced water splitting, the attachment of hydrogen to hydrocarbons as energy carriers and the reversible conversion of these chemical energies into a variety of other forms of energy, determining the activity of life. It is remarkable that

nature always utilizes electro-chemical energy as an intermediate in primary as well as secondary processes. It has to be emphasized that many complex energy-converting reactions can be catalyzed at ambient temperature or at low body temperature.

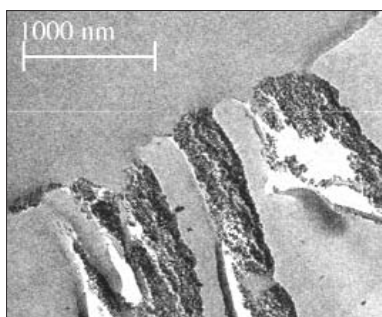


**Fig. 2:** Cross section of a polyethylene terephthalate (PET) membrane with pores filled with silica particles, the surface of which are covered by the proton-conducting amino acid layer (Lysin).

The aim of energy bionics is to learn from nature's energy technological paradigms. Prior to a technical application the natural mechanisms to be imitated have to be understood in detail. One conversion mechanism, nature has realized, concerns the effectiveness we know from fuel cells, i.e. the conversion of chemical into electrical energy. This active principle has already been realized in power plants of cells, the so-called mitochondria. Fuel cells consume oxygen for the same energy reason as human

beings in their respiration process.

The following cost-intensive components in PEM fuel cells were chosen to work out bionic solution strategies:

- replacement of platinum as electro-catalyst,
- development of alternative proton-conducting membranes,
- availability of hydrogen.

## Catalysts without noble metals.

Contrary to technical catalysts, frequently utilizing noble metals, nature has solved catalyst issues by applying abundant transition metals working at low temperatures. Cytochrome oxidase is a typical example demonstrating the conversion of oxygen into water as it occurs in fuel cells. Nature manages with iron, cobalt and copper centers, which become effective in an adapted molecular environment. It is eye catching that the metal centers in biological catalysts are surrounded by nitrogen, as it is the case in porphyrins or in the heme-groups (hemoglobin, myoglobin, different cytochromes). In the electron transferring B12 vitamin, cobalt is present in a similar nitrogen ligand field. Since single metal centers are not able to store several electrons at least two centers are coupled with each other allowing a fast and cooperative supply of electrons. These natural catalysts are distinguished by saturation of all kinds of bonding possibilities to protect themselves against oxidation processes.

The main bionic challenge is to maintain the central part of the catalytic center, replacing the organic environment (protein matrix) by inorganic groups. This is achieved by integrating the cores of iron and cobalt porphyrins in a nearly amorphous graphite matrix. To obtain a highly active surface iron oxalate was added as a foaming agent in the preparation process. By this means, the metal-nitrogen environment essentially remained unchanged. Figure 1 shows a transmission electron micrograph of a sponge-like catalytic particle with integrated cobalt-nitrogen cores. Even though the metal content of the catalysts is small (1–2 wt%) the catalytic activity is comparable to that of platinum [1].

## Proton-conducting membranes.

In PEM fuel cells expensive proton-conducting membranes on the basis of polytetrafluoro-ethylene-sulfonates (NAFION) are used. To find a natural analogon, mechanisms of proton con-

ductivity in nature have to be considered. In bacteriorhodopsin, for example, protons are conducted in channels, which are lined by amino acids. In a first approach, to mimic a bionic membrane, commercially available porous membranes have to be modified. From nanotechnology it is known that 15 nm sized silica particles can be attached at the surfaces of polymer channels. On the other hand, amino acids can be bonded via amino- or carboxyl-groups to the silica. Impregnating porous membranes by silica- and amino acid-containing solutions under vacuum, channels in the membranes were lined with amino acids as seen in the cross section of a transmission electron micrograph in Fig. 2. It could be demonstrated that these modified membranes exhibit protein conductivity in the order of commercial NAFION-membranes. Best results were obtained employing the amino acid lysine and porous polyethylene terephthalat (PET) [2].

### Tandem membrane for direct solar hydrogen evolution

In the process of photosynthesis plants do not collect current but convert light via electrochemical energy directly to fuel. While the direct photo-induced generation of fuels was seriously discussed after the first energy crisis in the seventies of the last century the efforts to learn from nature in this respect were superseded by the prospect of very cheap solar cells. However few research initiatives investigated the feasibility to collect sufficient energy in serially switched photovoltaic structures via two electron excitation to directly generate hydrogen from water omitting current collection and without use of a specialized electrolyser. The record in this field, obtained with the collaboration of our research group, achieved a solar efficiency of 18% concerning hydrogen evolution utilizing a tandem solar cell of 20% efficiency [3]. This result shows that 90% of the photovoltaic energy can directly be converted into hydrogen applying adjusted catalysts. This yield is impressive when compared with the efficiency of photosynthesis cultivating sugar cane where even at three harvests per year only an mean efficiency of 0.5% can be obtained related to the conversion of light into chemical energy in form of biomass. However, the solar cell structures used based on the semiconductors gallium arsenid and silicon cannot be put offhand in contact with water. Therefore, to technically realize a photosynthetic membrane materials are in demand which are reactive in water, but at the same show long term stability.

It is well known for 30 years that  $\text{TiO}_2$  absorbing ultraviolet light from the sunlight can oxidize water under oxygen evolution. During this process che-

mical radicals will be formed that can also be used to oxidize organic molecules to  $\text{CO}_2$  and water. This property has been used in the last time with increasing interest to produce self-cleaning surfaces. Recently, as it was reported that carbon- and nitrogen-doped  $\text{TiO}_2$  layers can shift the photosensitivity in the range of visible light it seemed to be time for the development of a water stable membrane mimicking photosynthesis. Figure 3 shows the concept pursued at the Hahn-Meitner-Institut. A titanium foil is oxidized at the one side adding an appropriate dopand and a suited catalyst. At the other side of the foil a simplified  $\text{CuInS}_2$  solar cell is deposited by reactive sputtering. Replacing the highly conductive  $\text{ZnO}$  layer by  $\text{TiO}_2$  no current collecting layer is any more necessary. In this way a membrane is available which is confined at both sides by a thermo-dynamically stable  $\text{TiO}_2$  layer. Electrons extracted from water at the one side will be excited in two steps in the  $\text{TiO}_2$  and the  $\text{CuInS}_2$  layer passing to the opposite side where they will react with water under evolution of hydrogen. Unfortunately, the shift of the band gap of carbon- and nitrogen-doped  $\text{TiO}_2$  layers in the visible range allowing water oxydation at lower energies could not be verified in our own electrochemical investigation using Differential Electrochemical Mass Spectroscopy (DEMS) [4]. Therefore, further research activities are needed to tailor an adapted oxide material with suitable band gap for this in principle functioning type of fuel generating photovoltaic membrane.

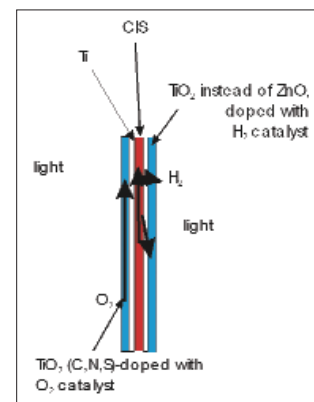


**Fig. 3:** Photosynthetic membrane composed of two confining  $\text{TiO}_2$  layers, a titanium foil as substrate and a light absorbing  $\text{CuInS}_2$  layer.

- [1] P. Bogdanoff, I. Herrmann, M. Hilgendorff, I. Dorbandt, S. Fiechter, H. Tributsch, *New Materials for Electrochemical Systems*, **7**, 85–92 (2004)
- [2] H.-J. Leem, J. Rojas-Chapana, S. Fiechter, H. Tributsch, *Bio-Analogue Amino Acid Lined Proton Conducting Channel for Fuel Cell Membranes*, in prep.
- [3] S. Licht, B. Wang, S. Mukerji, T. Soga, M. Umeno, H. Tributsch, *Efficient Solar Water Splitting, Exemplified by  $\text{RuO}_2$ -Catalyzed  $\text{AlGaAs/Si}$  Photoelectrolysis*, *J. Phys. Chem. B* **104**, 8920–8924 (2000)
- [4] B. Neumann, P. Bogdanoff, H. Tributsch, S. Sakthivel, H. Kisch, *Electrochemical Mass Spectroscopic and Surface Voltage Studies of Catalytic Water Oxidation by Undoped and Doped Titania*, *J. Phys. Chem B.*, handed in

### Corresponding author:

H. Tributsch  
tributsch@hmi.de

# Spectromicroscopy: investigating the ALILE process

W. Bremsteller<sup>1</sup>, C. Lehmann<sup>1</sup>, T. Plake<sup>1</sup>, C. Pettenkofer<sup>1</sup>, J. Schneider<sup>2</sup>, J. Klein<sup>2</sup>, M. Muske<sup>2</sup>, S. Gall<sup>2</sup>

■ 1 HMI, SE6 ■ 2 HMI, SE1

Thin crystalline silicon solar cells have the potential for very high efficiencies. This has been shown by the preparation of a solar cell with an efficiency of 21.5% on a thinned-down monocrystalline Si wafer [1]. Unfortunately this is not a real Si thin-film but still a Si wafer technology. It is expected that only real Si thin-film manufacturing, which uses for example large-area glass substrates, can lead to a significant cost reduction on a long term. Such a thin-film technology requires the preparation of Si layers on glass with high structural and electronic quality by an industrially applicable process. The use of glass limits the processing temperatures to about 600°C. Thus, much interest has been focussed on amorphous Si (a-Si) as a precursor for polycrystalline Si (poly-Si) in a solid phase crystallization process which involves annealing temperatures of about 600°C. The use of metals can be favourable to achieve lower annealing temperatures as well as larger grain sizes. Nast *et al.* have demonstrated that aluminium-induced crystallization (AIC) of a-Si can be used to prepare large-grained poly-Si films on glass by annealing a glass/Al/a-Si stack and thus transforming it into a glass/poly-Si/Al+Si stack, as depicted in Fig. 1 [2]. Hence, it is called Al-induced layer exchange (ALILE) process.

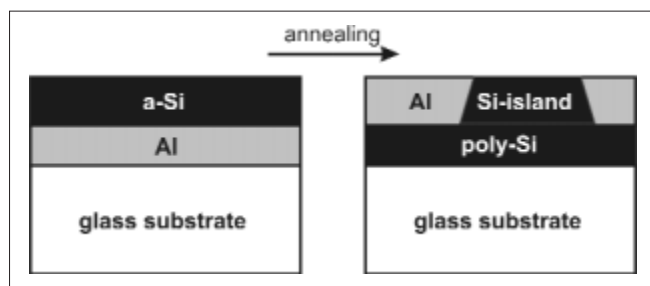


Fig. 1: Schematic of the ALILE process

The ALILE process can be easily observed in-situ in an optical microscope (e.g. [4]). However, it remains an open task to distinguish the grown structures by their chemical composition, i.e. to observe the annealing process in some kind of spectromicroscopy. At the Berlin electron synchrotron facility BESSY, we are able to resolve the chemical constituents of a sample surface using our photoemission electron microscope (PEEM) [3]. Hereby, electrons excited by a monochromated light beam having an energy of at least the sample's work function are emitted from the sample surface and subsequently imaged as in conventional electron microscopy. In the image plane, a microchannel plate is mounted to render the impinging electrons visible. An additional energy filter in the microscope column allows a selection of the electrons by their kinetic energy. In combination with monochromated x-ray light up to  $h\nu=1000\text{eV}$  as provided by the BESSY undulator beamline U49/2 we were able to compose the PEEM image only of core electrons of the selected chemical species.

With the equipment at hand, we were able to study the ALILE process. Prior to PEEM investigations, the samples were inserted into the preparation chamber and  $\text{Ar}^+$  sputtered for 90 min to remove the oxide from the a-Si top layer. Subsequently, a complete ALILE annealing process was carried out at 460°C for about 12 hours. Figure 2 presents the resulting sample surface contrast in the photoelectron micrographs. In Fig. 2a bright islands are visible which are areas of  $\text{Si}2p$  photoelectron emission, i.e. those Si islands shown in Fig. 1. In a complementary fashion, the  $\text{Al}2p$  emission stems from the area around the Si islands (Fig. 2b). Thus, we have found direct evidence for the chemical composition of the stack top layer after the layer exchange due to annealing.

Since XPEEM is able to produce integral real-time images within its field of view we were interested in the time-dependent change of the sample surface as the annealing process takes place. Figure 3 depicts a series of PEEM spectromicrographs generated with an excitation energy of  $h\nu=200.0$  eV. The detection energy of the microscope is alternately set to Al2p (binding energy  $E_B=74.1$  eV) and Si2p ( $E_B=99.5$  eV). As the temperature is gradually increased from room temperature to a maximum of 380°C over a period of 3 hours, the homogeneously bright Si2p image starts to exhibit randomly distributed dark islands, i.e. areas with absence of Si (cf.  $t_0$ , Fig. 3). Changing the detection energy to Al2p emission these islands can be clearly identified as Al. Initially, the diameter of those features is in the order of 1  $\mu\text{m}$ . From only a few of these islands Al starts to spread laterally until the Si is dissolved ( $t_0+35$  min, Fig. 3). The compact silicon islands detected in Fig. 2 would be formed upon persistent annealing due to Oswald ripening.

While optical microscopy is limited in resolution and to reflection analysis of the samples XPEEM offers much higher resolution of only a few nanometers as well as direct access to the chemical composition of the surface layer. We have succeeded in laterally resolved direct analysis of the chemical composition during an ALILE annealing process. The observations carried out demonstrate the vast potential of the photoemission electron microscope opera-

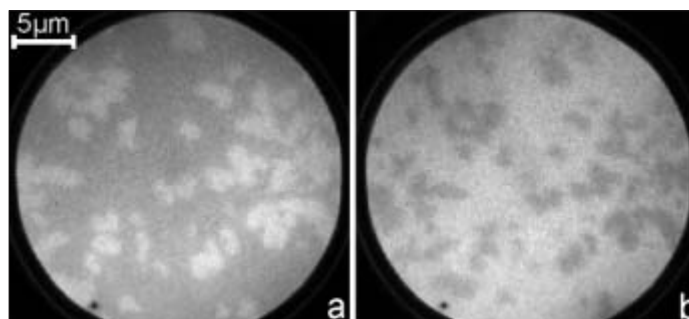


**Fig. 2:** Complementary photoelectron micrographs of a glass/300 nm Al/375 nm a-Si stack annealed for about 12 hours at 460°C. Bright areas represent (a) Si2p, (b) Al2p core level emission.

ted at the Berlin electron synchrotron to determine the chemical constituents and their lateral distribution in the surface of a planar sample. Having started with the investigation of the ALILE process we are certain that a number of groups will benefit from our PEEM analysis experimental setup in the future.

- [1] J. Zhao, *et al.* in: Proceedings of the 13<sup>th</sup> European Photovoltaic Solar Energy Conference, Nice, France, 1566 (1995)
- [2] O. Nast, *et al.*, Appl. Phys. Lett. **73**, 3214 (1998)
- [3] <http://www.elmitec.de/html/peem.html>
- [4] J. Schneider *et al.*, J. Non-Cryst. Solids **338–340**, 127 (2004)

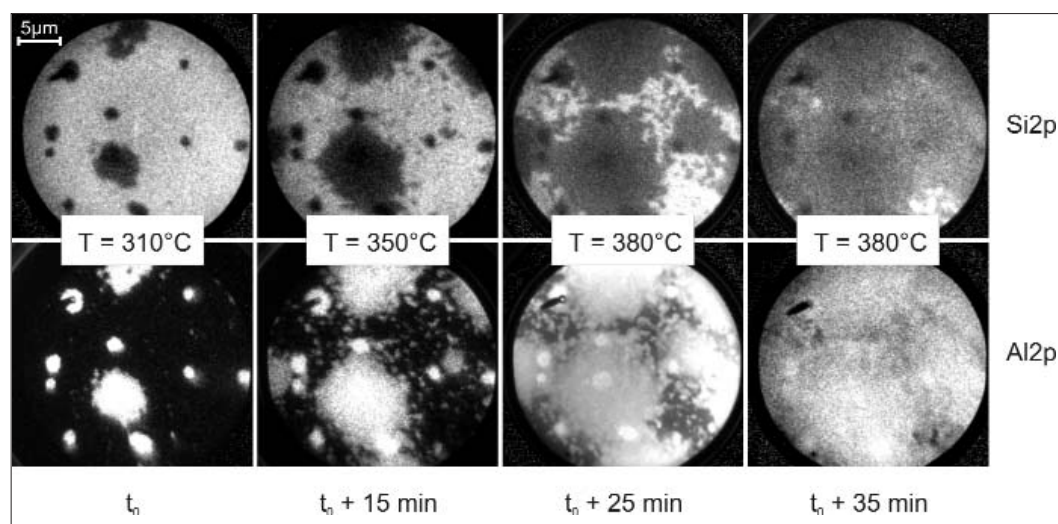


**Fig. 3:** ALILE process of a 300 nm Al/375 nm a-Si stack on glass during a period of 35 minutes. In the upper/lower row, bright areas correspond to Si2p/Al2p core level emission.

**Corresponding author:**

T. Plake  
plake@hmi.de

# Band structure and effective masses for CuInS<sub>2</sub>

C. Lehmann, W. Calvet, T. Plake, R. Hunger, C. Pettenkofer

■ HMI, SE6

Understanding the interface properties in heterogeneous solar cell junctions demands a firm understanding of the electronic structure of the materials involved. CuInS<sub>2</sub> is used as an absorber material in thin film cells. However, only little experimental work is reported on the valence band structure of chalcopyrites [1]. For example, it is possible to deduce the effective mass  $m^*$  from the valence band curvature. Along with the bulk band structure, one is also interested in the occurrence of surface states which may play a key role for the formation of intergap states at the interfaces of such a device.

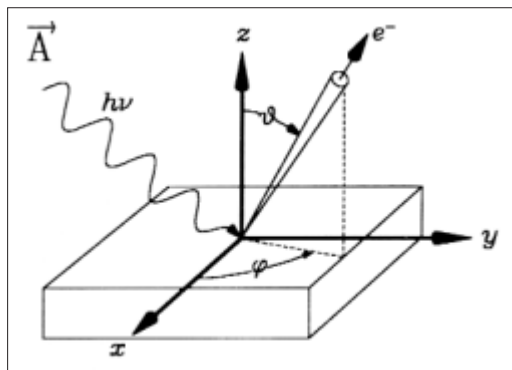


**Fig. 1:** Illustration of angle resolved photoemission spectroscopy

Angle resolved photoemission spectroscopy (ARPES) is the technique of choice to map the band structure of conductive solid states such as metals and semiconductors. In principle, an electron energy analyser is scanned across the half space of the sample surface which emits photoelectrons excited by an ultraviolet monochromated light source. For the latter, synchrotron radiation is desirable since it provides high photon flux, variable energies, and a well-defined polarisation vector. ARPES requires the knowledge of the crystal orientation, which can be determined by low-energy electron diffraction (LEED). Thus, one can scan the electron analyser stepwise along lines of high symmetry. For each step a kinetic energy spectrum of the photoexcited valence electrons is recorded.

From the position of the emission maxima and the detection angles (cf.  $\varphi$  and  $\theta$  in Fig. 1) the valence band structure can be deduced.

At the Berlin electron synchrotron laboratory (BESSY) we run an ARPES machine (ADES/SoLiAS) at the TGM7 beamline with energies ranging from 6 eV to 35 eV and 25 eV to 120 eV. The experimental setup consists of several modules for preparation, sample treatment and analysis under ultrahigh vacuum (UHV) conditions.

One of the major difficulties in CuInS<sub>2</sub> is to obtain well-defined, smooth and clean crystal surfaces. We have chosen a cleaving method in UHV, which may be an elaborate task since only one out of ten samples yields satisfying results. However, the advantage of this procedure is to obtain pure and unstrained crystal surfaces which allow direct comparison with theoretical band structure calculations (e.g. [2]). For this work, we used CuInS<sub>2</sub> crystals that were grown in a Bridgeman process. Crystallites at a size of the order 5 mm × 5 mm × 5 mm were glued to the sample holder and cleaved in UHV.

Once a sample has been successfully cleaved it is checked by LEED for both the crystal quality and orientation. With this information, the sample is brought into position for photoemission spectroscopy. Figure 2 depicts a series of photoemission spectra for scanning from (112) to (110) direction at excitation energies of  $h\nu = 20$  eV and  $h\nu = 27$  eV. Hereby, the (inverted) second derivatives of the spectra are merged into a colour scale plot to facilitate a visible impression of the valence band structure. Values for  $k$  have been obtained via the equation

$$k_{\parallel} = \sqrt{\frac{2m_e}{\hbar^2} E_{kin}} \sin\theta \quad m_e = \text{electron mass}$$

The band closest to binding energy  $E_B=0\text{ eV}$  is the valence band edge with a maximum at the  $\Gamma$  point, i.e. for a vanishing component of the  $k$  vector parallel to the sample surface ( $k_{\parallel}=0$ ). Between binding energies of 2 eV and 5 eV, a number of highly dispersive bands can be seen. According to theory, those bands originate from Cu3d and S3p states. Separated at about  $E_B=7\text{ eV}$ , In-S bonds form a common band. Since the excitation energy is varied in both plots, the vertical component  $k_{\perp}$  of  $k$  is effected as well. Thus, both plots represent different cuts through  $k$ -space.

In order to determine the effective mass  $m^*$  at the centre of the Brillouin zone  $\Gamma$  we fitted the maximum of the valence band edge with a parabola  $E_B=f(k)$  as depicted in Fig.3. From the fit parameters, we obtain via

$$\frac{1}{m^*} = \frac{1}{\hbar^2} \frac{f^2 E}{fk^2}$$

an effective mass for the chalcopyrite  $\text{CuInS}_2$  of

$$|m^*/m_e|=0.45 \pm 0.06$$

In summary, we have presented unprecedented measurements of the valence band structure of a bulk  $\text{CuInS}_2$  crystal. From the curvature of the valence band maximum we determined the effective mass of the material as  $m^*=0.45 m_e$ , which is similar to other semiconductor compounds such as GaAs. The information obtained here will later be compared to the electronic structure of epitaxial  $\text{CuInS}_2$  films, which is subject to ongoing research.

- [1] R. Hunger *et al.*,  
BESSY annual report (2004)  
[2] J.E. Jaffe, A. Zunger,  
Phys. Rev. B **28**, 5822 (1983)

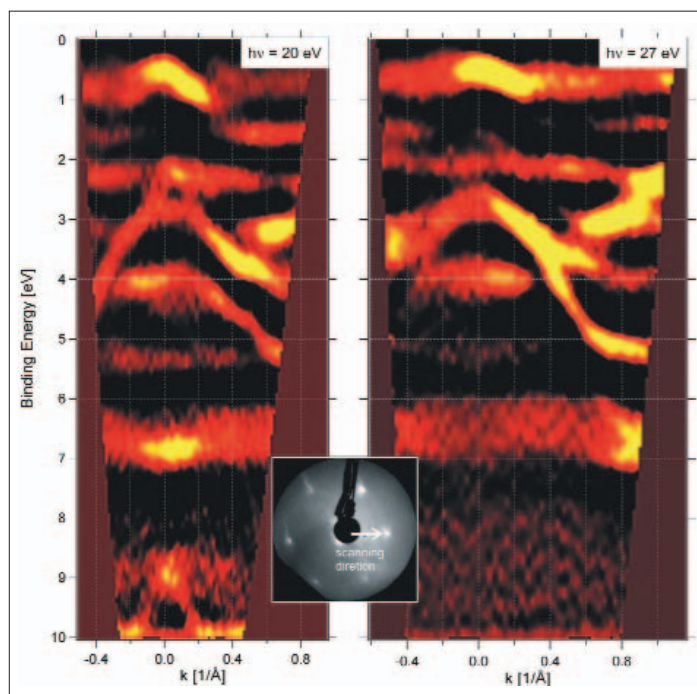


**Fig. 2:** Colour scale plots of the  $\text{CuInS}_2$  valence band structure along a high symmetry path in the (112) face determined by angle resolved photoemission spectroscopy for two different excitation energies  $h\nu=20\text{ eV}$  (left) and  $h\nu=27\text{ eV}$  (right). Bright regions correspond to minima of the second derivative of the spectra.

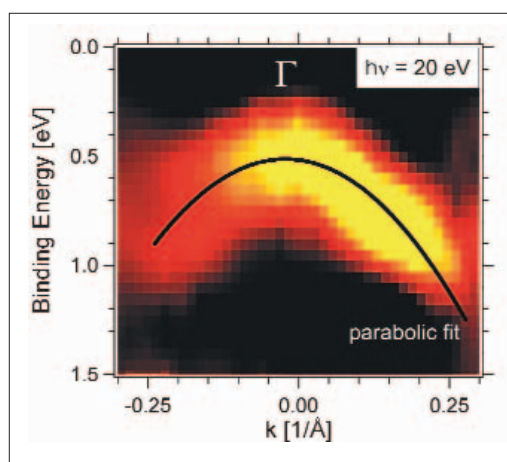


**Fig. 3:** Parabolic fit of the valence band maximum for determining the effective mass  $m^*$ .